Electronic Supplementary Information

Tunable Third-Order Nonlinear Optical Effect via Modifying Ti$_4$(embonate)$_6$ Cage-Based Ionic Pairs

*Guang-Hui Chen, Yan-Ping He *, Zi-Rui Wang, Qiao-Hong Li, Zhi-Zhou Ma, and Jian Zhang ***

G.-H. Chen, Y.-P. He, Z.-R. Wang, Q.-H. Li, Z.-Z. Ma, J. Zhang

State Key Laboratory of Structural Chemistry, Fujian Institute of Research on the Structure of Matter, Chinese Academy of Sciences, Fuzhou, Fujian 350002, P. R. China.

E-mail: hyp041@163.com; zhj@fjirsm.ac.cn

Y.-P. He

University of Chinese Academy of Sciences, Beijing 100049, P. R. China.

E-mail: hyp041@163.com

Contents

1. The PXRD Analyses for PTCs

Figure S1. The PXRD patterns of simulated from the single-crystal data of **PTC-293** (black), as-synthesized **PTC-293** (red).
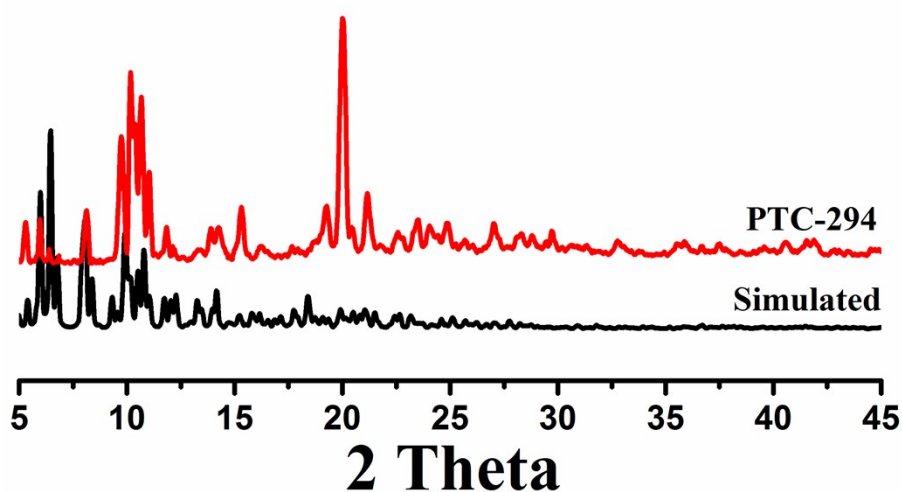
Figure S2. The PXRD patterns of simulated from the single-crystal data of **PTC-294** (black), as-synthesized **PTC-294** (red).
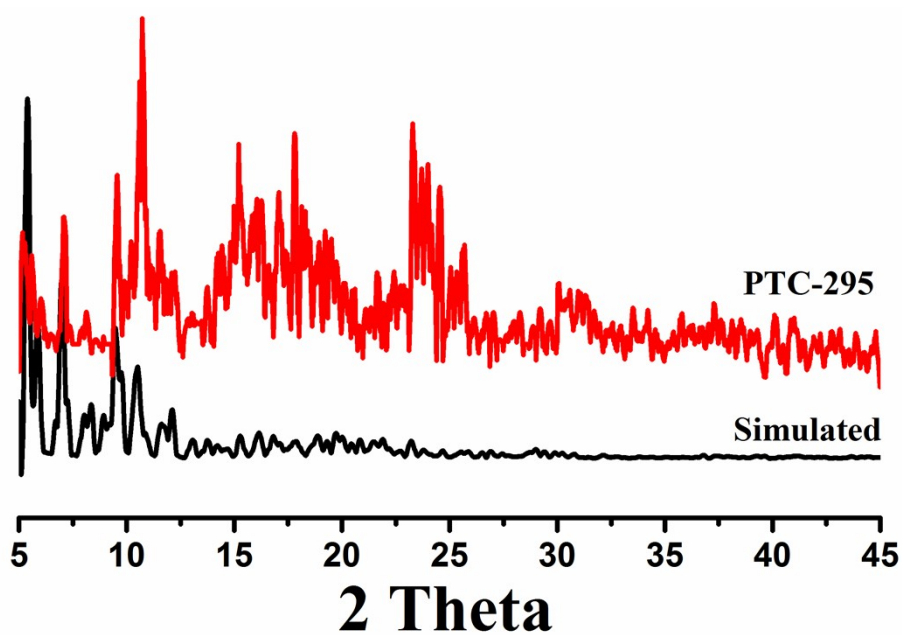
Figure S3. The PXRD patterns of simulated from the single-crystal data of **PTC-295** (black), as-synthesized **PTC-295** (red).
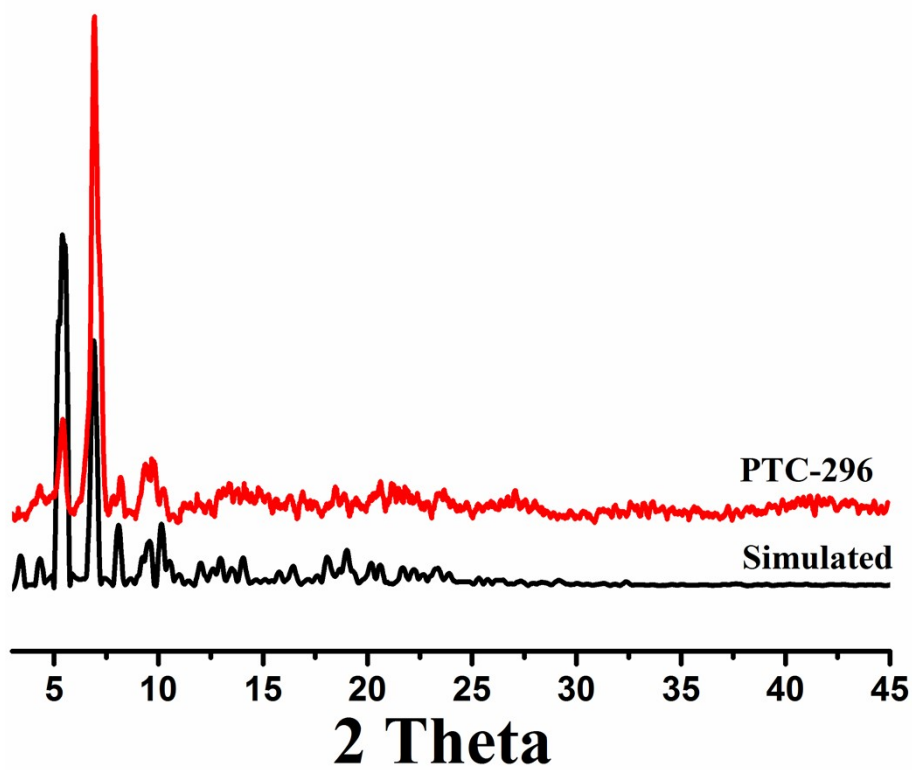
Figure S4. The PXRD patterns of simulated from the single-crystal data of **PTC-296** (black), as-synthesized **PTC-296** (red).

2. Detailed Structure Information for PTCs.
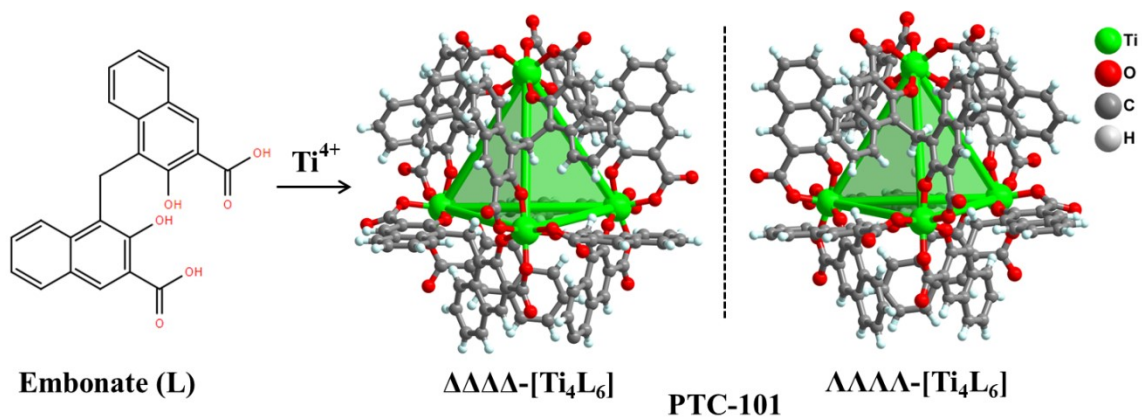
Figure S5. Illustration of the structures of the embonate (L) ligand, the $\Delta\Delta\Delta\Delta$-[Ti$_4$L$_6$] and $\Lambda\Lambda\Lambda\Lambda$-[Ti$_4L_6$] isomers in PTC-101.[1]
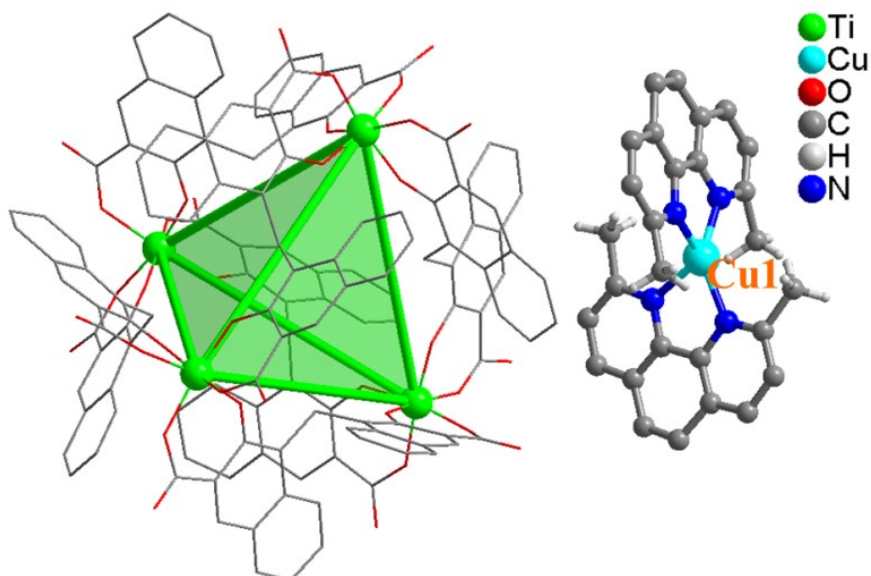
Figure S6. The asymmetric unit of **PTC-293**, showing one Ti$_4$L$_6$ cage, one [Cu(Me$_2$phen)$_2$]$^+$ cation and some free (NH$_4$)$^+$ cations which could not be located because of highly disorder.
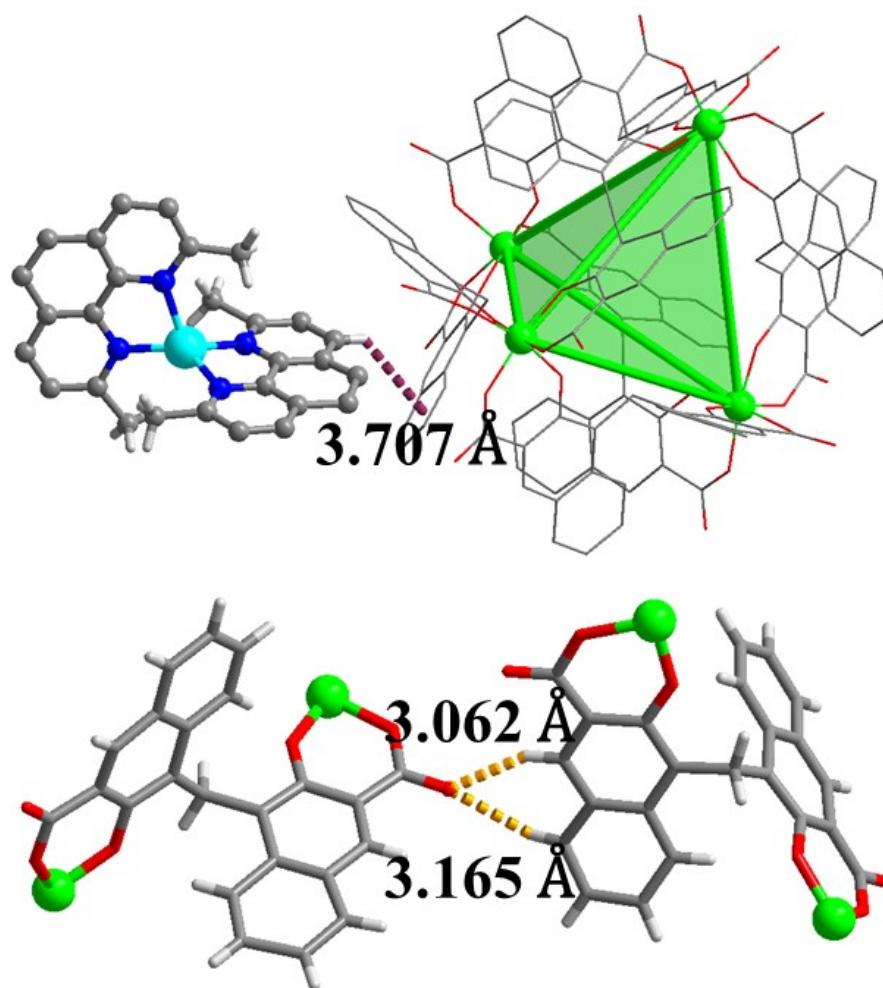
Figure S7. The highlighting of the C−H⋯π and the C−H⋯O weak interactions between adjacent Ti$_4$L$_6$ cage and [Cu(Me$_2$phen)$_2$]$^+$ cation or two Ti$_4$L$_6$ cages, respectively.
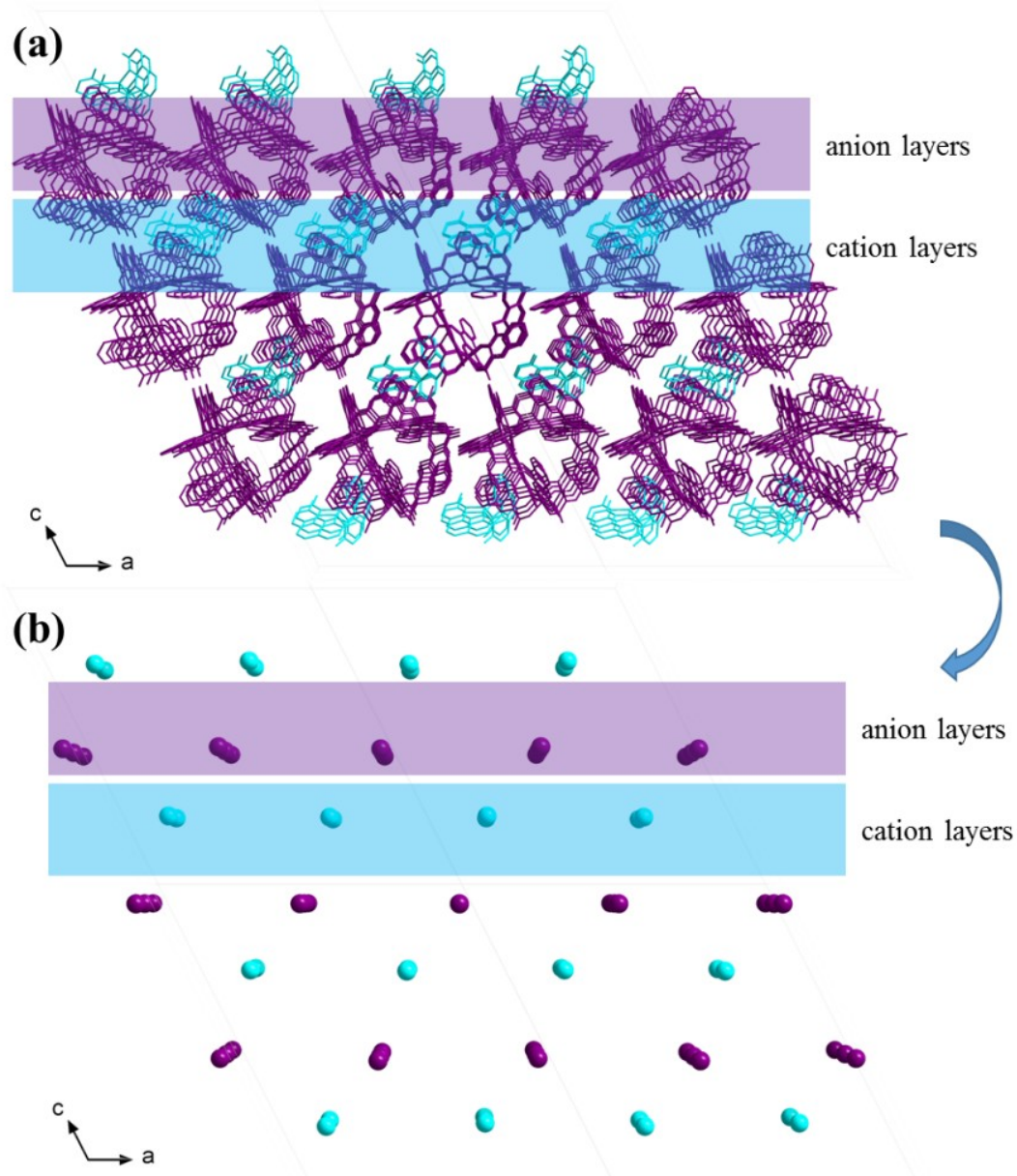
Figure S8. (a) Molecular packing diagram of **PTC-293** co-crystals projected along the crystallographic b-axis. (b) Schematic illustration of $Ti_4(embonate)_6$-based ionic pairs methodology with conventional parallel-type cation–anion assembly with alternating cation and anion layers.
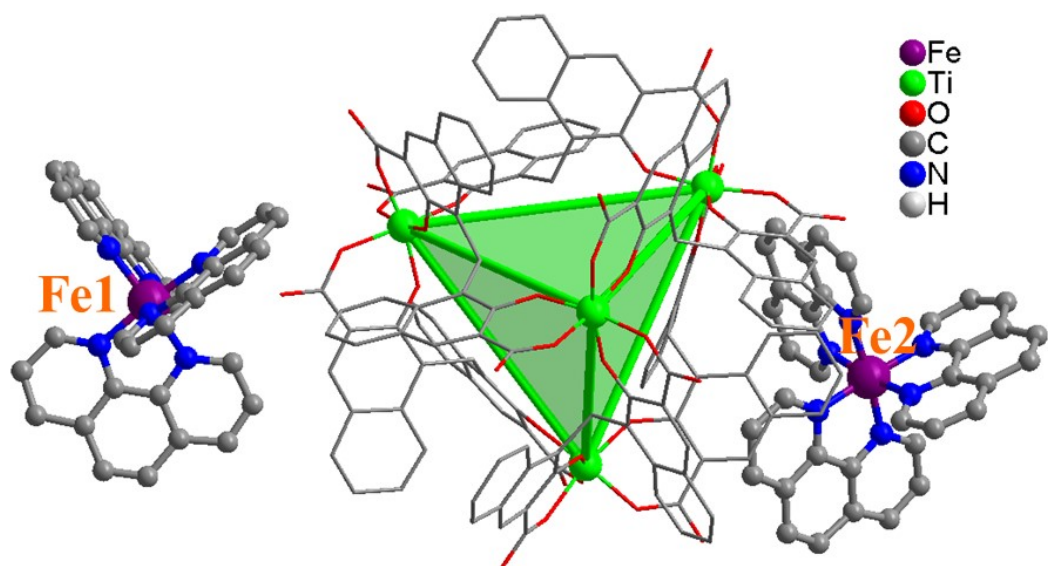
Figure S9. The asymmetric unit of **PTC-294**, showing one Ti_4L_6 cage, two $[Fe(phen)_3]^{2+}$ cations, and some free $(NH_4)^+$ cations.
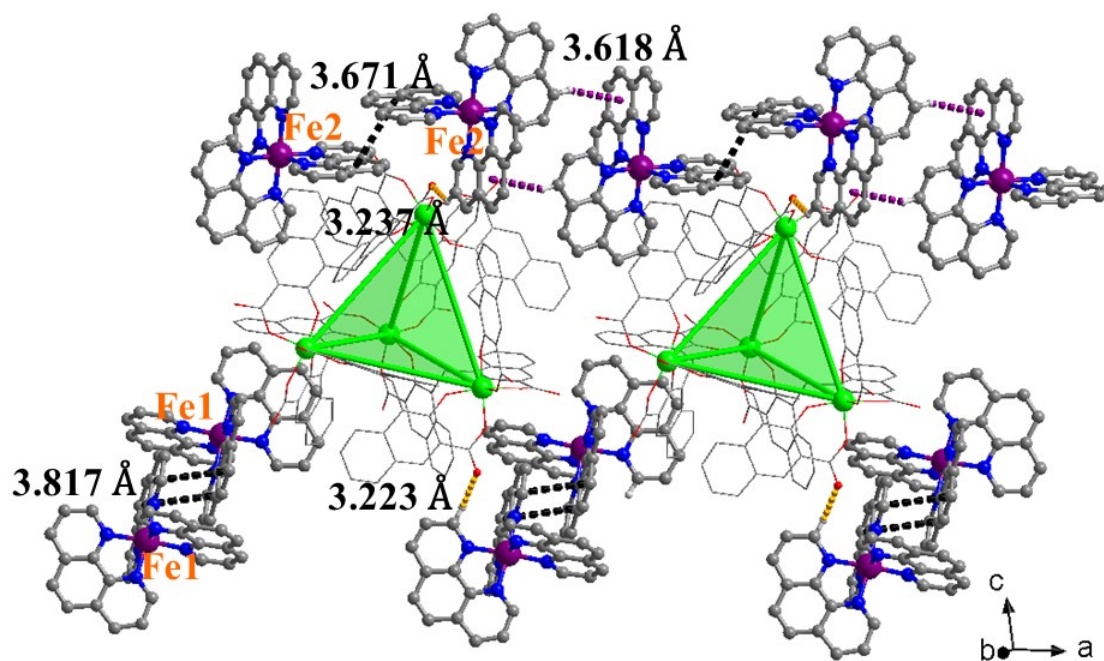
Figure S10. The highlighting of the $\pi\cdots\pi$ stacking and C−H$\cdots\pi$ interactions between adjacent $[Fe(phen)_3]^{2+}$ cations as well as the C−H$\cdots$O hydrogen bonds between adjacent Ti_4L_6 cage and $[Fe(phen)_3]^{2+}$ cation, respectively.
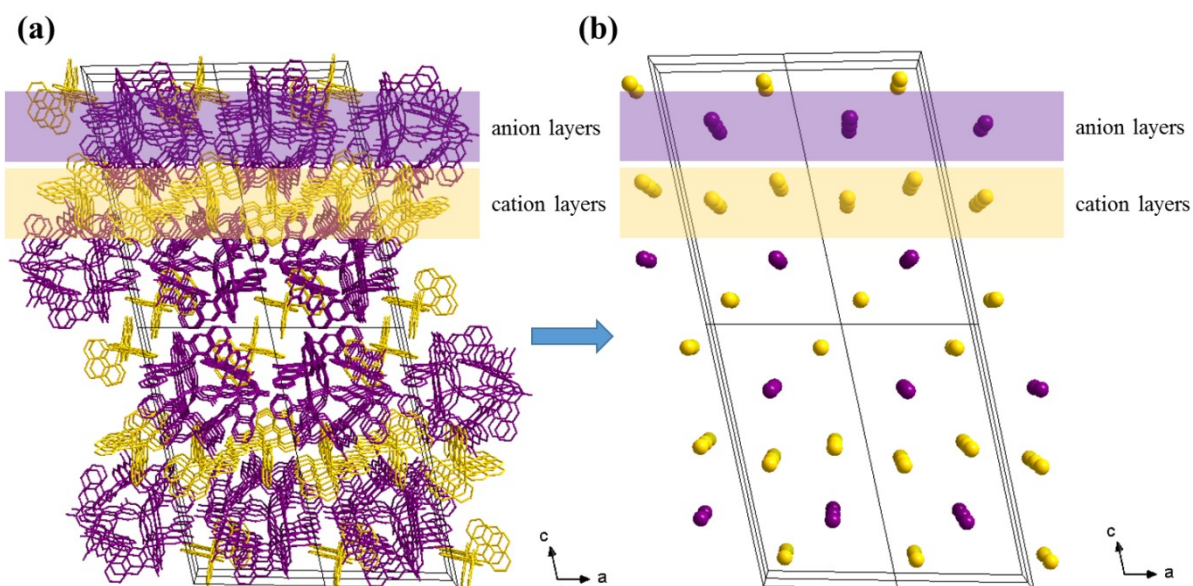
Figure S11. (a) Molecular packing diagram of **PTC-294** co-crystals projected along the crystallographic b-axis. (b) Schematic illustration of $Ti_4(embonate)_6$-based ionic pairs methodology with conventional parallel-type cation–anion assembly with alternating cation and anion layers.
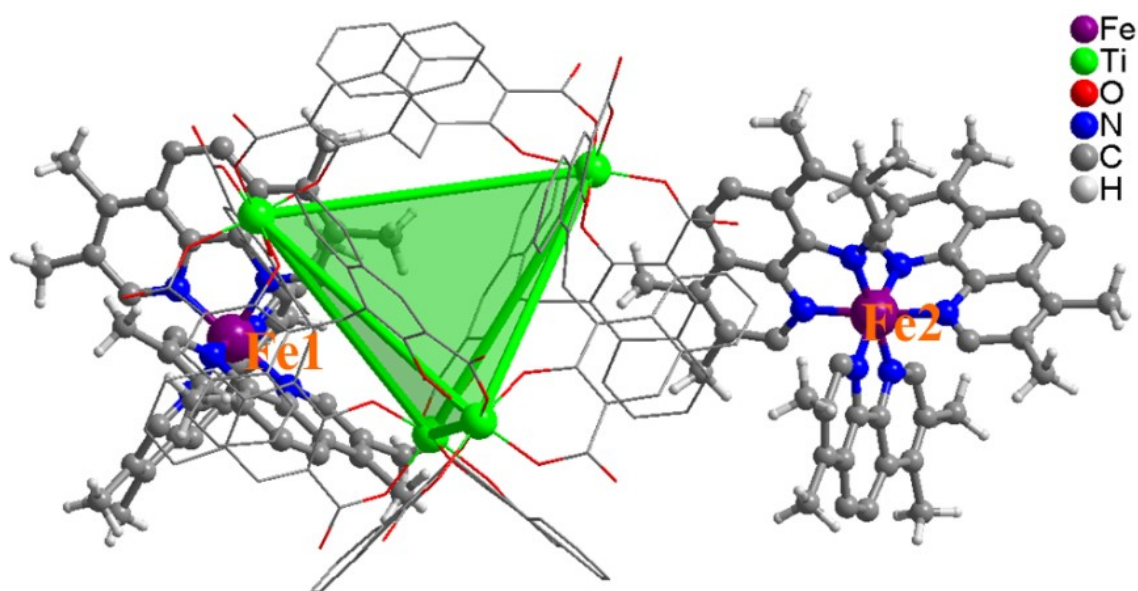
Figure S12. The asymmetric unit of **PTC-295**, showing one Ti_4L_6 cage, two $[Fe(Me_4phen)_3]^{3+}$ cations and some free $(NH_4)^+$ cations.

(3.9-4.4 Å)
π···π interactions

C−H···π interactions
(3.3-3.9 Å)
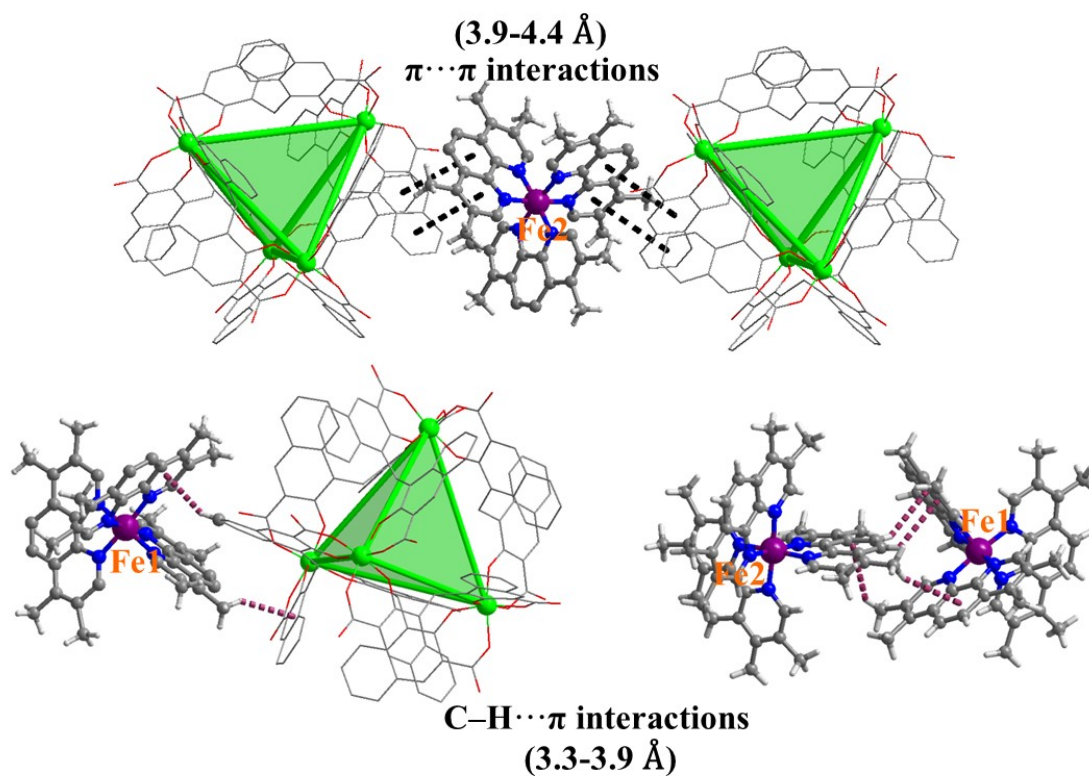
Figure S13. The highlighting of the π···π stacking and C−H···π interactions between adjacent Ti_4L_6 cage and $[Fe(Me_4phen)_3]^{3+}$ cation.
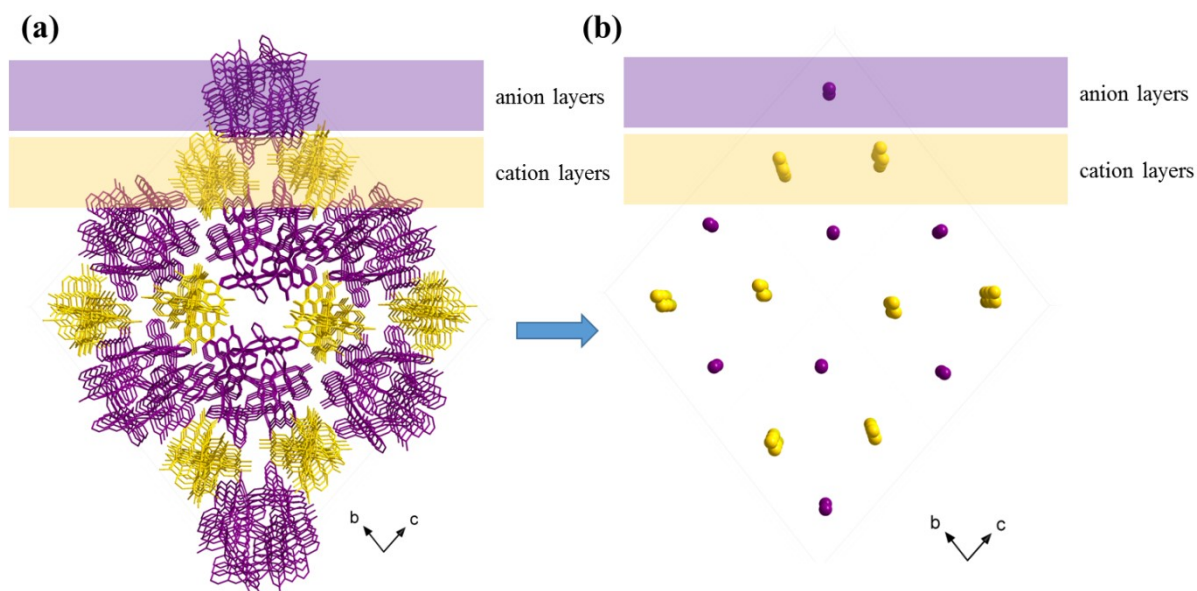
Figure S14. (a) Molecular packing diagram of **PTC-295** co-crystals projected along the crystallographic a-axis. (b) Schematic illustration of $Ti_4(embonate)_6$-based ionic pairs methodology with conventional parallel-type cation–anion assembly with alternating cation and anion layers.

10
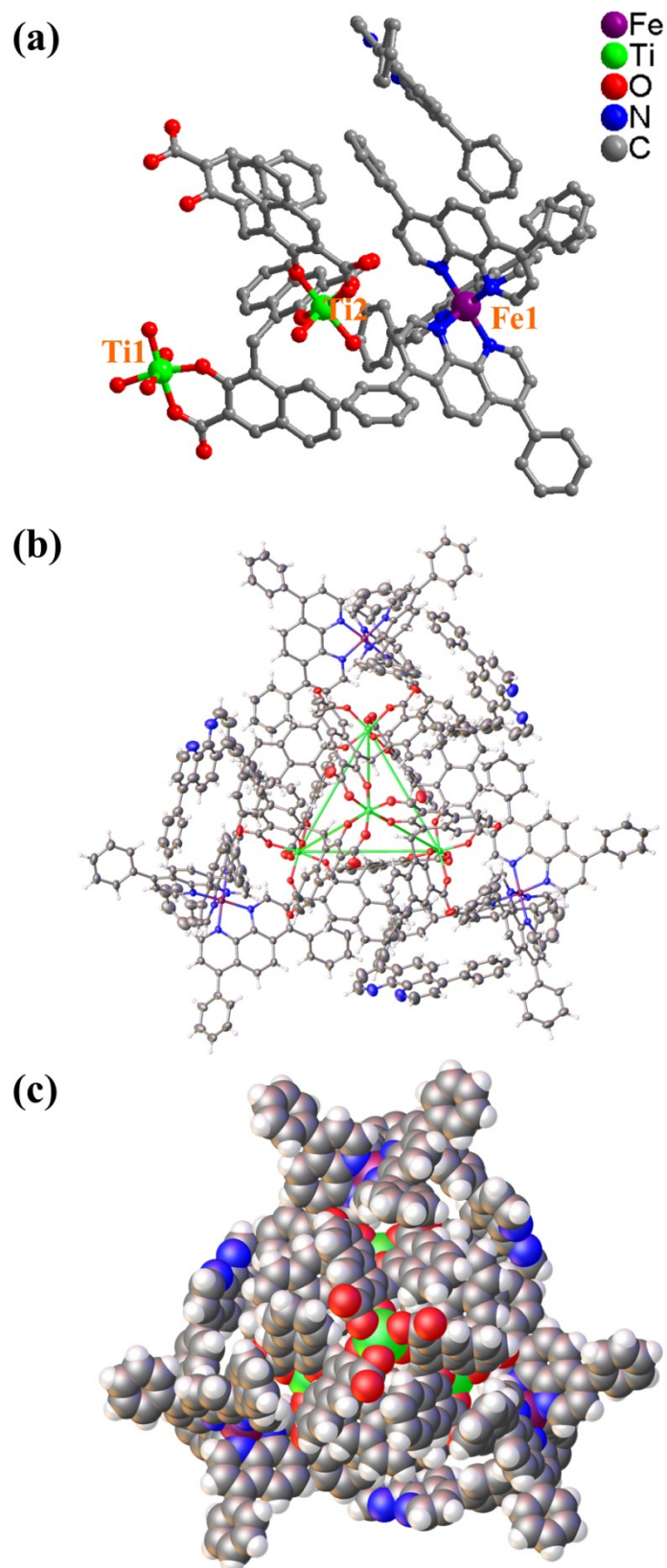
Figure S15. (a) The asymmetric unit of **PTC-296**, showing one third of Ti_4L_6 cage and one $[Fe(Ph_2phen)_3]^{3+}$ cation, one Ph_2phen ligand and some free $(NH_4)^+$ cations. (b) ORTEP diagram for **PTC-296** with the ellipsoids drawn at the 30% probability level. (c) Sphere packing representations of the **PTC-296**.
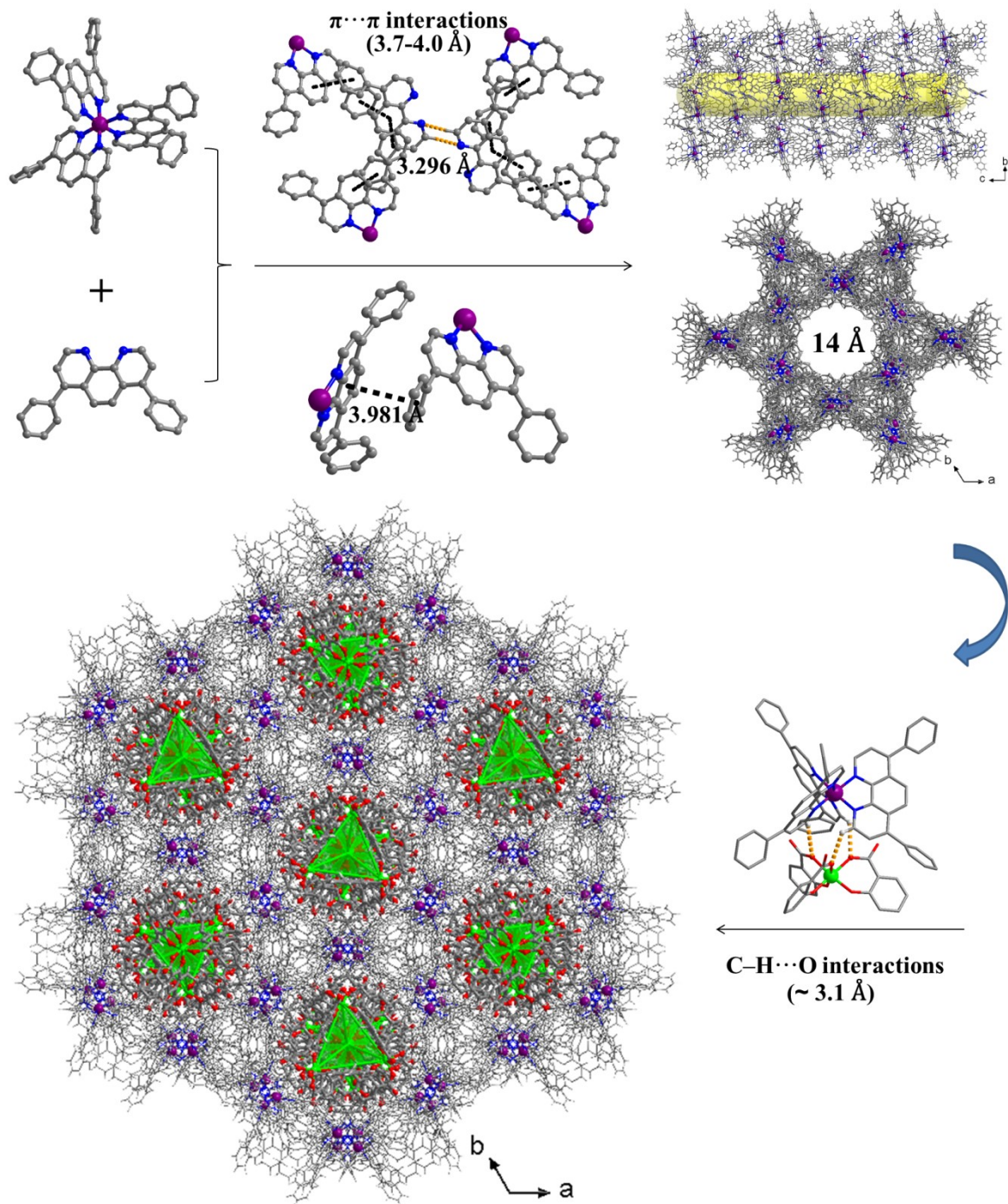
Figure S16. Structural assembly process of **PTC-296**. Atom color code: green, Ti; cyan, Cu; modena, Fe; red, O; blue, N; gray, C; offwhite, H.

π-π interactions (3.7-4.0 Å)
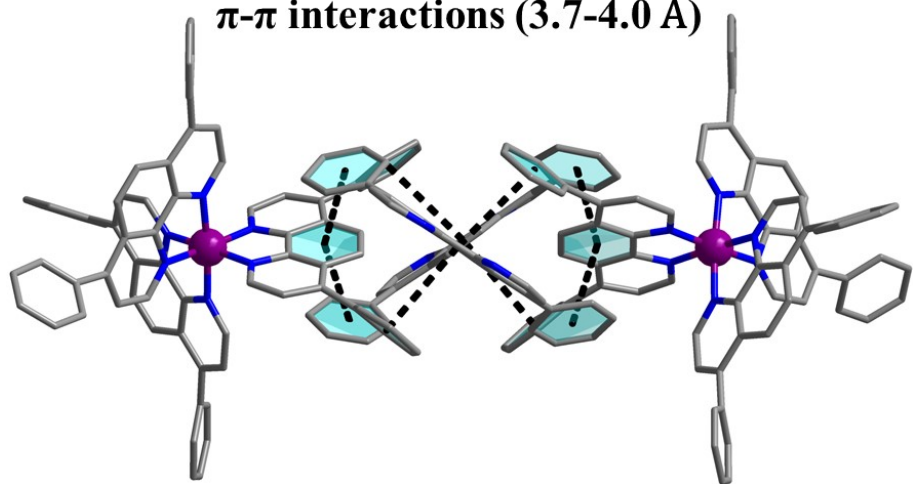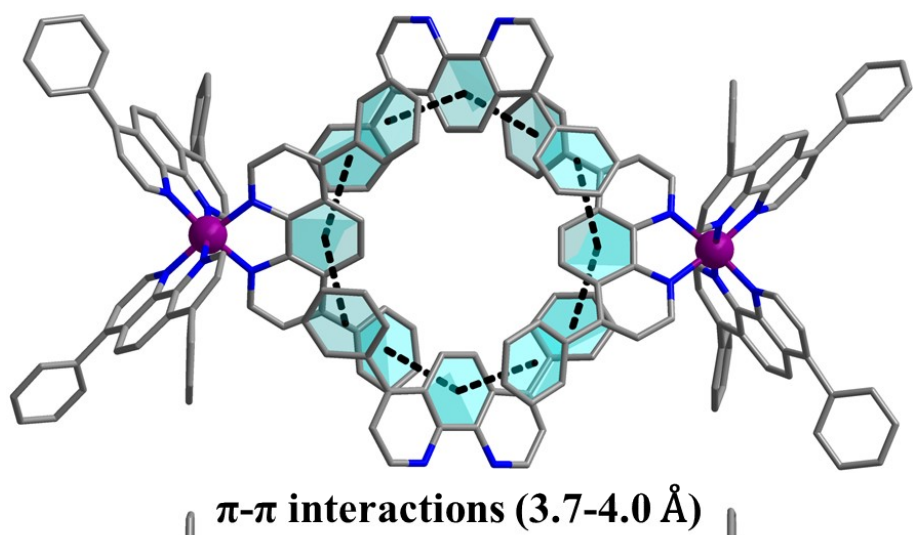
Figure S17. The schematic diagram of π···π in **PTC-296**.

C−H···π interactions (3.5-3.8 Å)
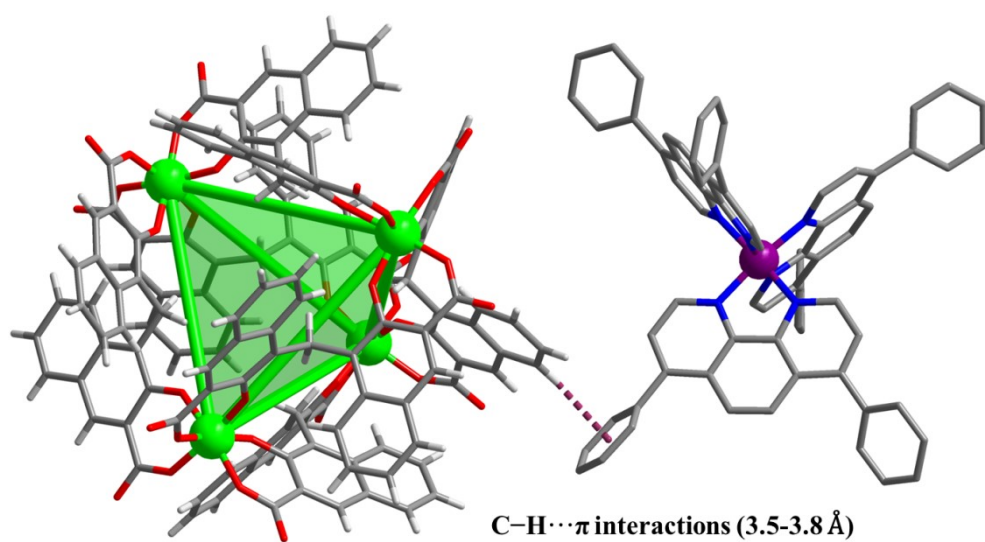
Figure S18. The schematic diagram of C-H···π in **PTC-296**.
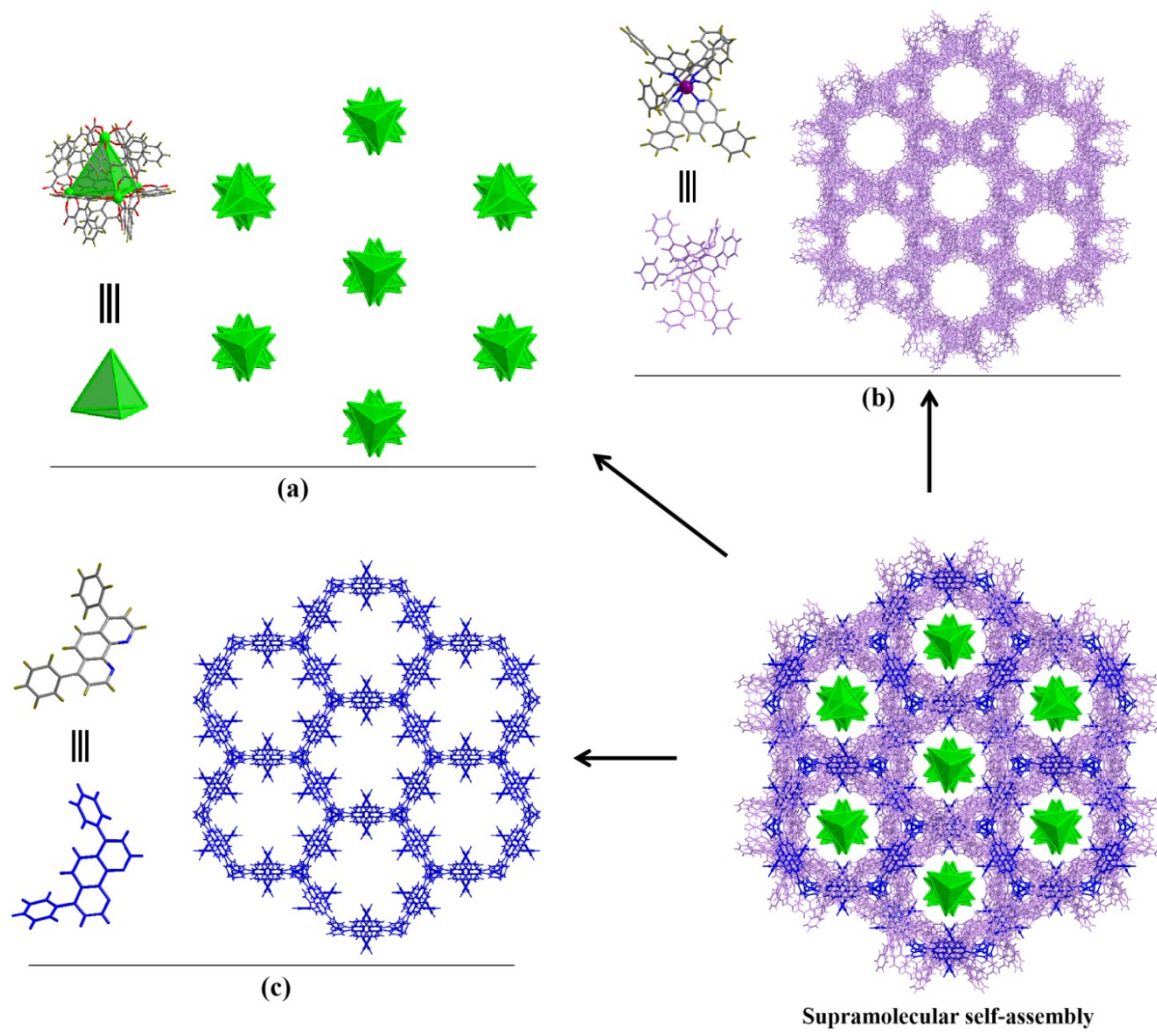
Figure S19. Illustration the intergration of Ti_4L_6 cage, Ph_2phen ligand and $[Fe(Ph_2phen)_3]^{3+}$ unit into a 3D supramolecular architecture of **PTC-296**.
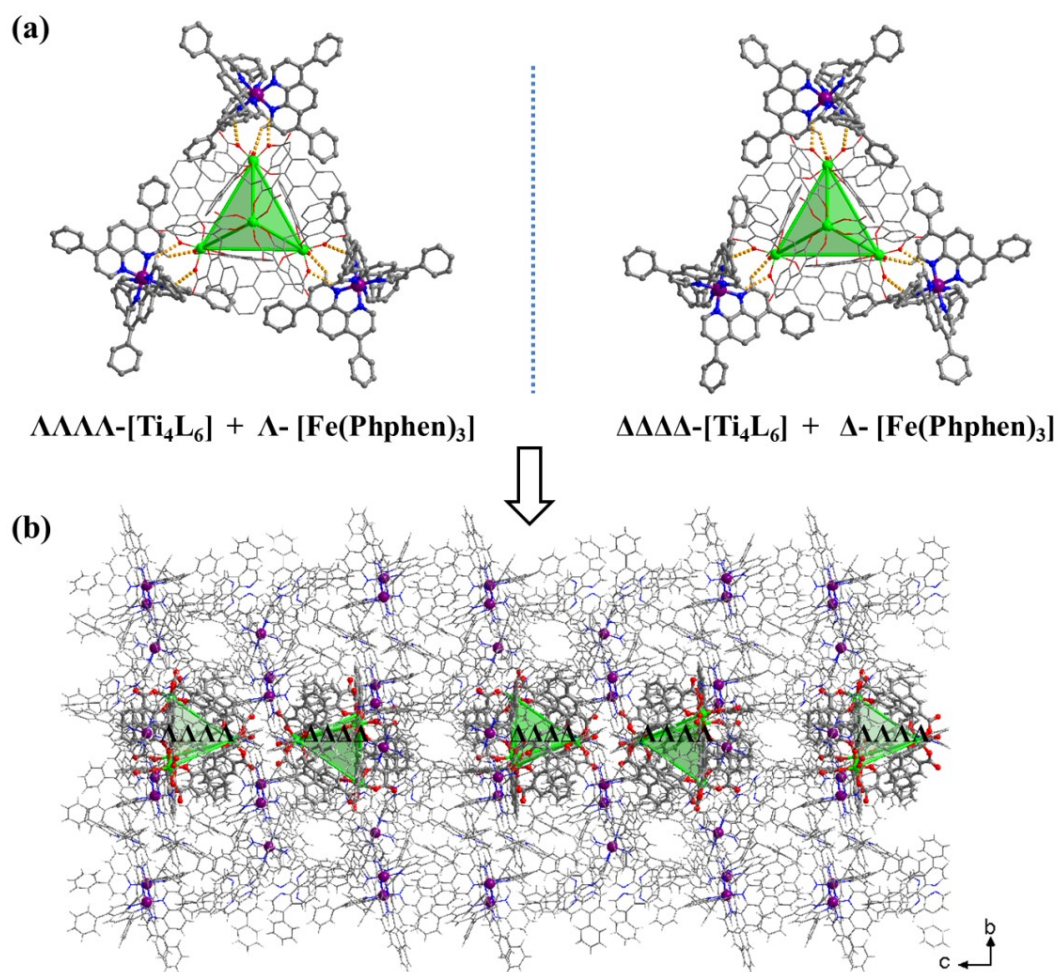
Figure S20. (a) Matching between the calixarene-like oxygen vertices of the Ti$_4$L$_6$ cage and the [Fe(Ph$_2$phen)$_3$]$^{3+}$ unit through C−H···O hydrogen bonds in **PTC-296**; (b) the 3D packing superstructure of **PTC-296** along the a-axis direction.
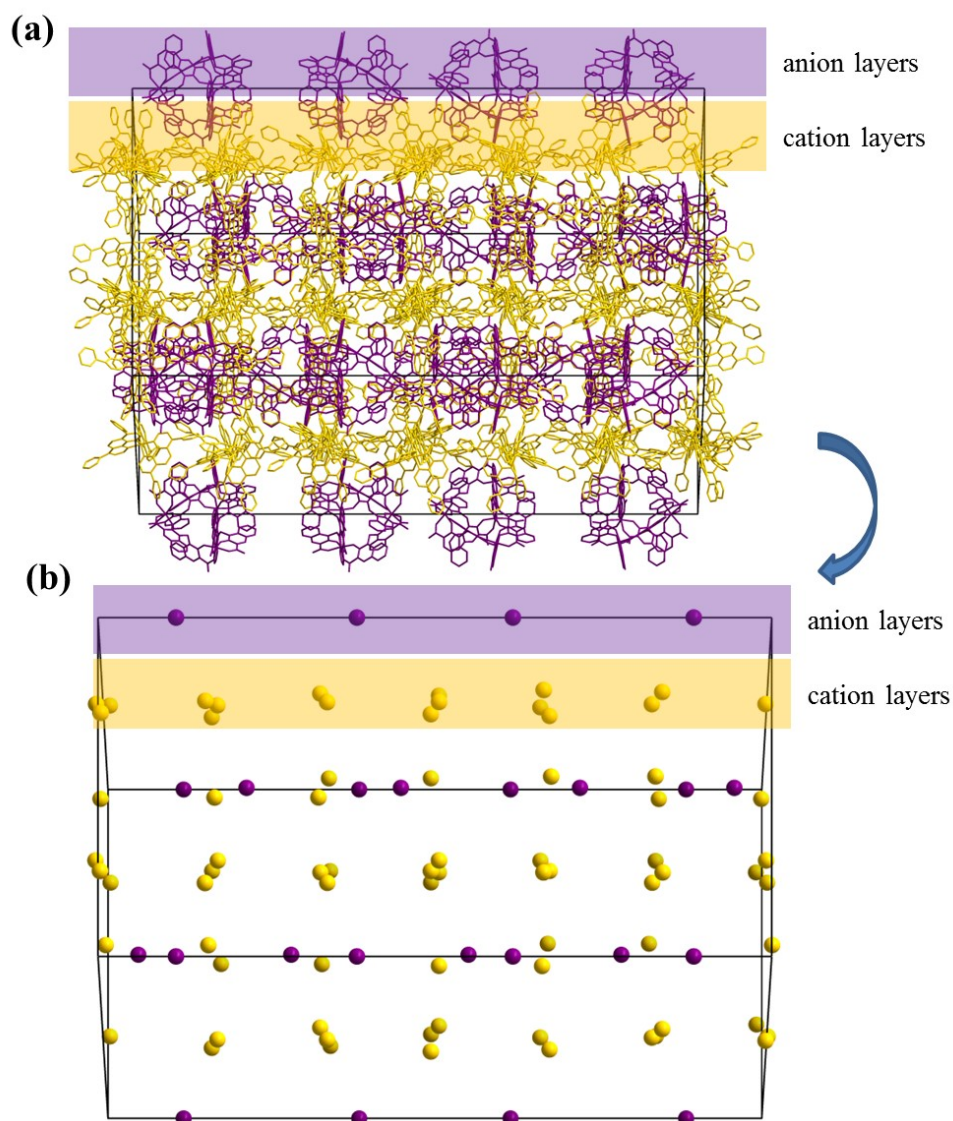
Figure S21. (a) Molecular packing diagram of **PTC-296** co-crystals projected. (b) Schematic illustration of $Ti_4(embonate)_6$-based ionic pairs methodology with conventional parallel-type cation–anion assembly with alternating cation and anion layers.

16

3. The SEM-Mapping Spectra of PTCs
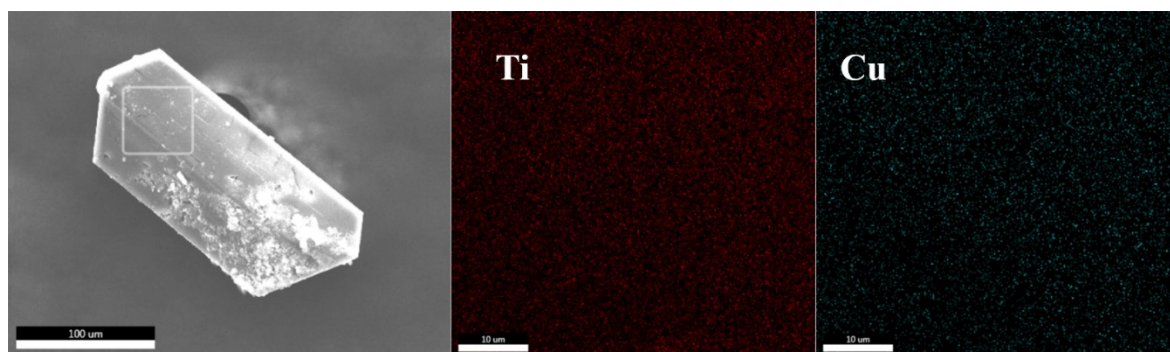
Figure S22. The SEM-mapping spectra of **PTC-293**. From left to right are crystal appearance, titanium, and copper elements.
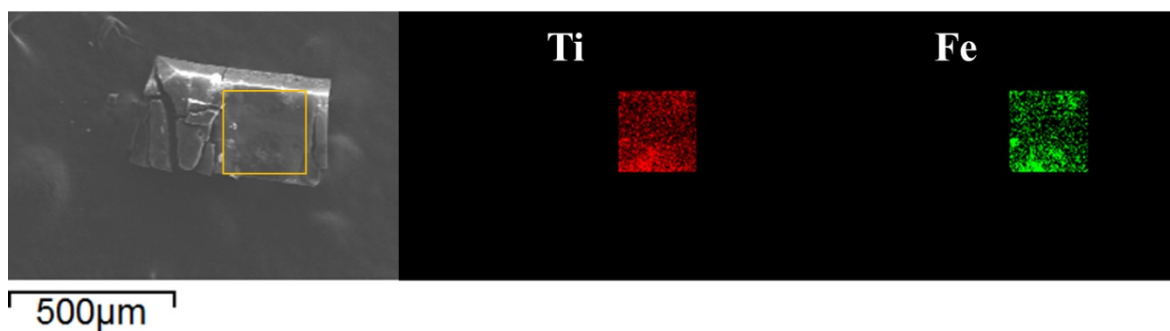
Figure S23. The SEM-mapping spectra of **PTC-294**. From left to right are crystal appearance, titanium, and iron elements.
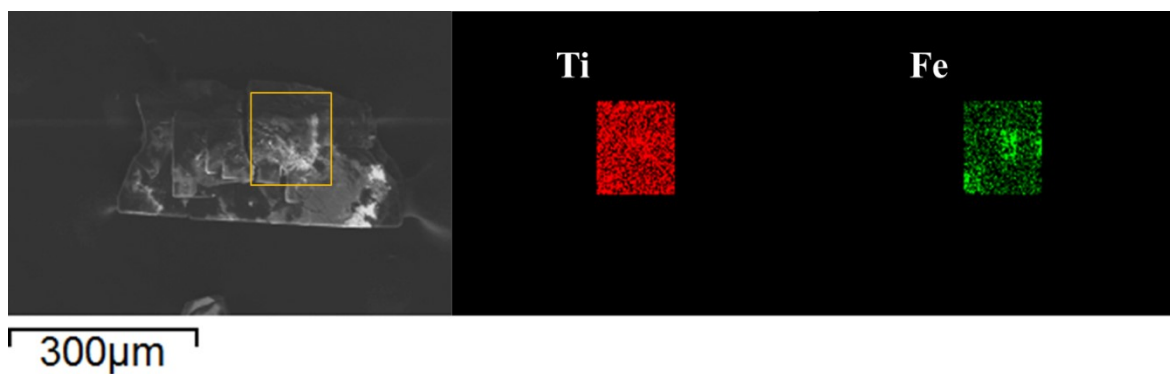
Figure S24. The SEM-mapping spectra of **PTC-295**. From left to right are crystal appearance, titanium, and iron elements.
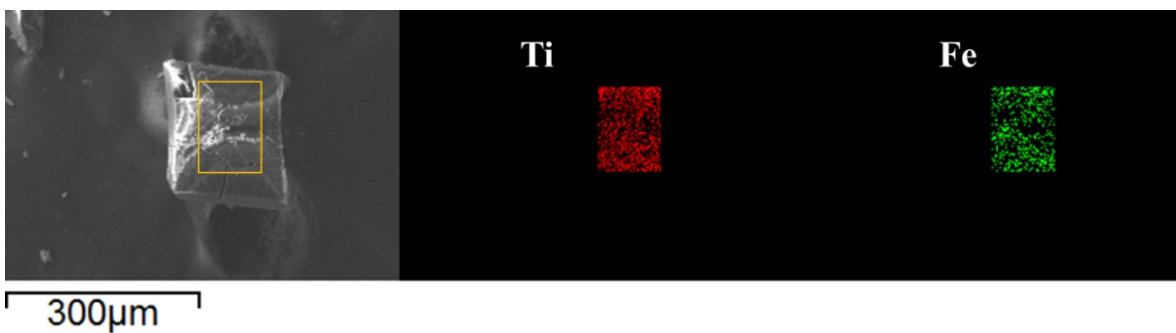
Figure S25. The SEM-mapping spectra of **PTC-296**. From left to right are crystal appearance, titanium, and iron elements.

4. The EDS Spectra of PTCs

Lsec: 15.0 0 Cnts 0.000 keV Det: Octane Plus Det
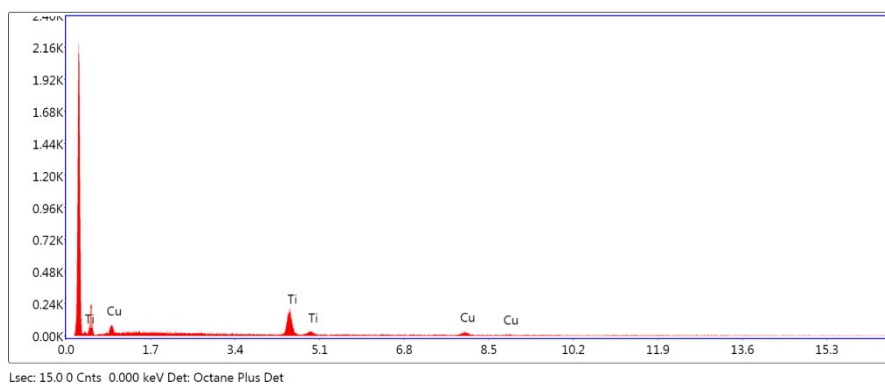
Figure S26. The EDS spectrum of compound **PTC-293**.
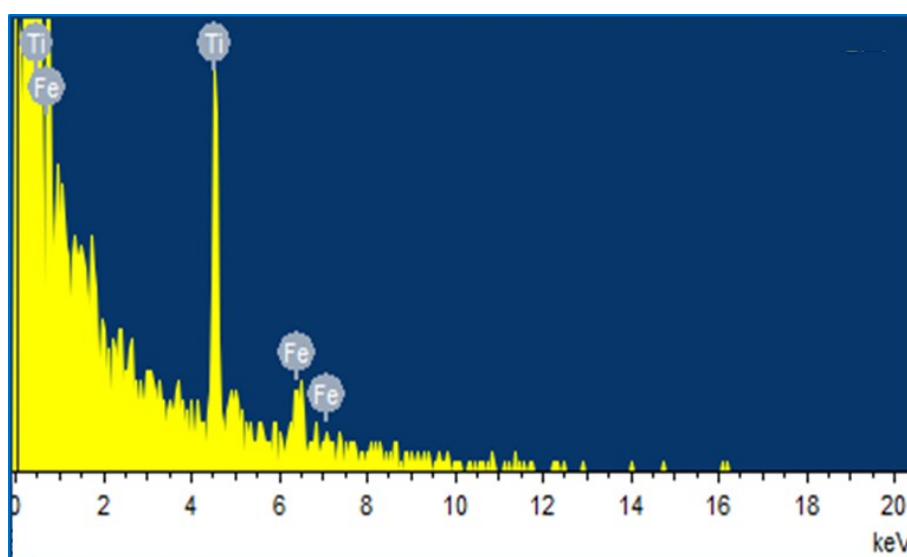
Figure S27. The EDS spectrum of compound **PTC-294**.
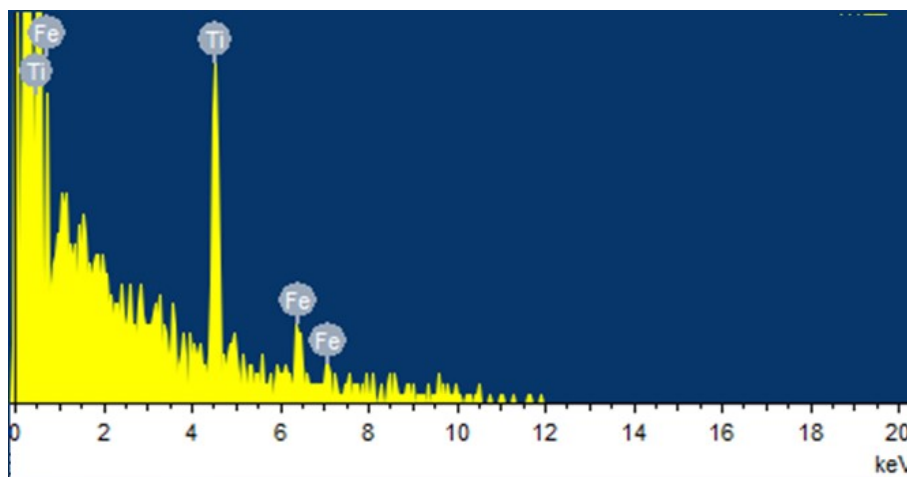
Figure S28. The EDS spectrum of compound **PTC-295**.
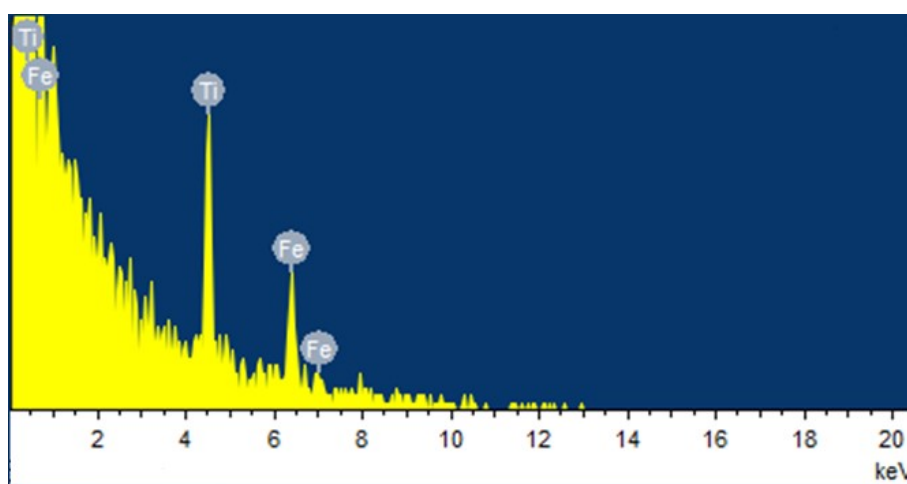
Figure S29. The EDS spectrum of compound **PTC-296**.

5. The UV-Vis Spectra of PTCs
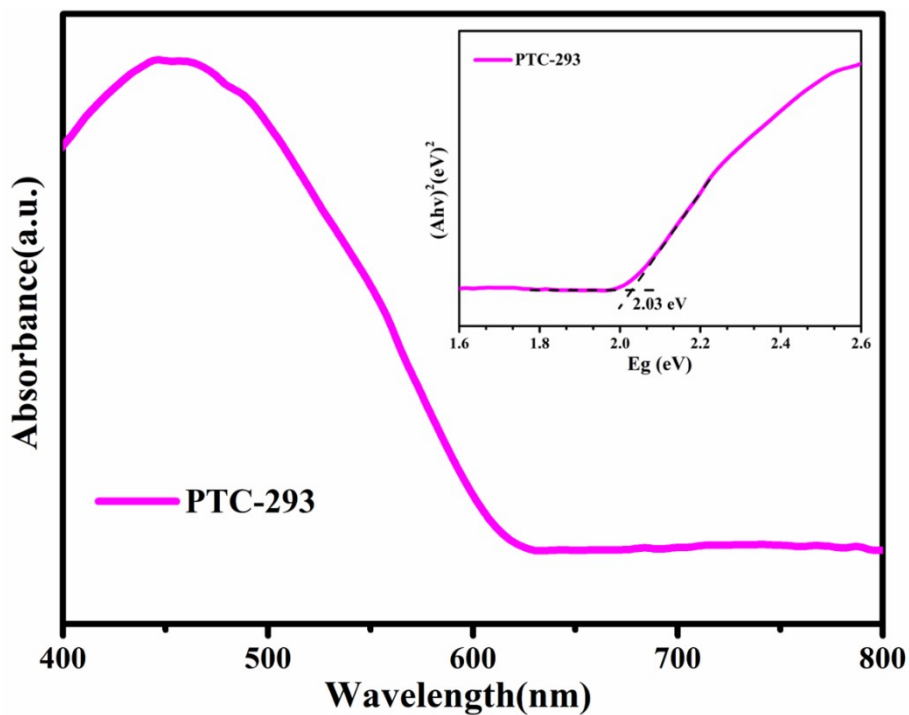
Figure S30. The solid-state UV absorption spectra of **PTC-293**.
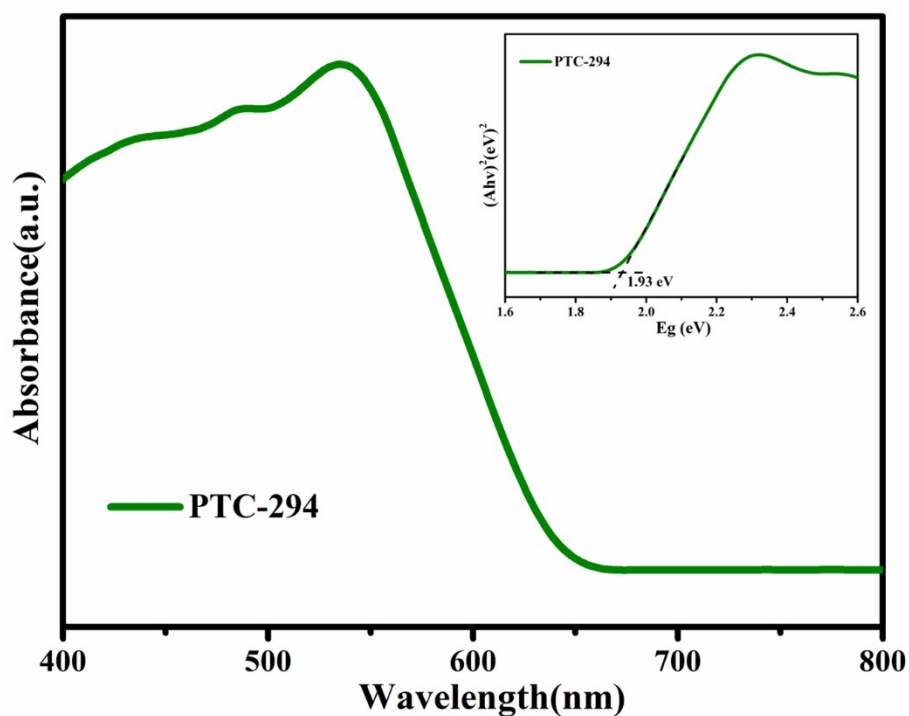
Figure S31. The solid-state UV absorption spectra of **PTC-294**.
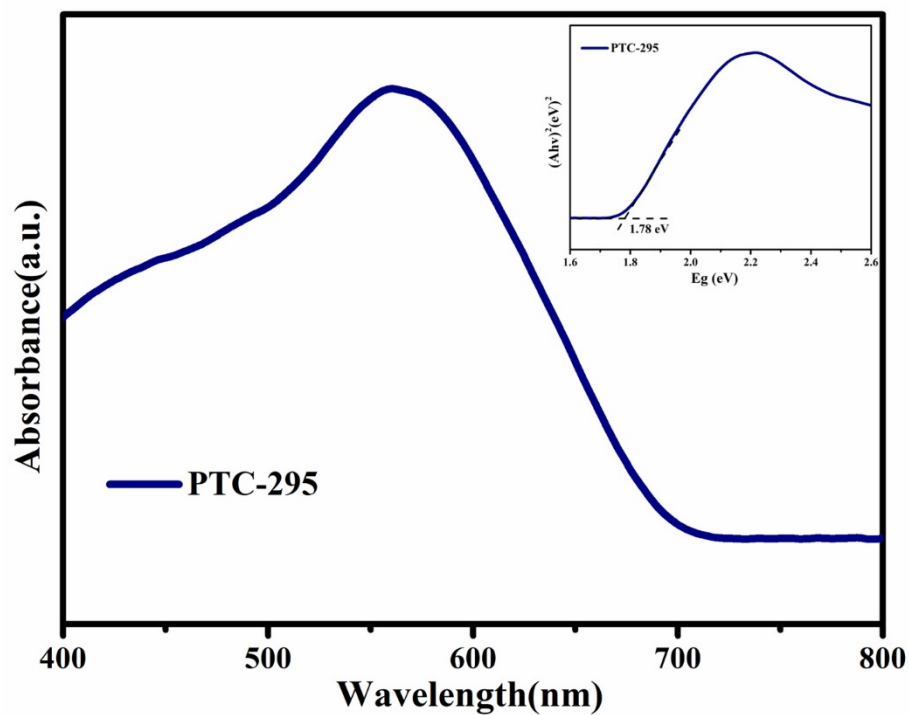
Figure S32. The solid-state UV absorption spectra of **PTC-295**.
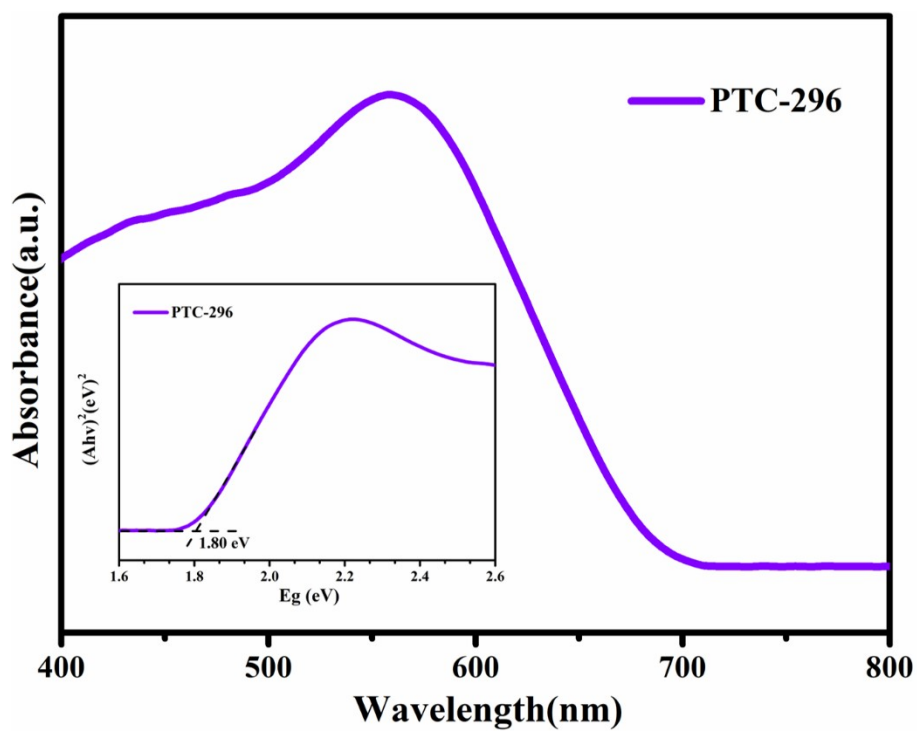
Figure S33. The solid-state UV absorption spectra of **PTC-296**.
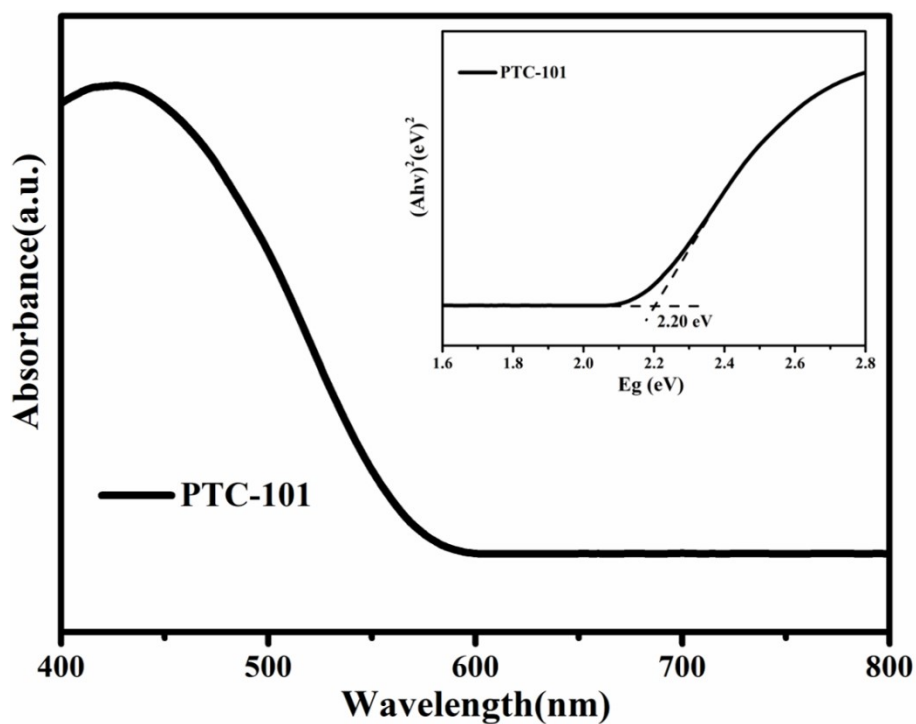
Figure S34. The solid-state UV absorption spectra of PTC-101.

6. The FT-IR Spectra of PTCs
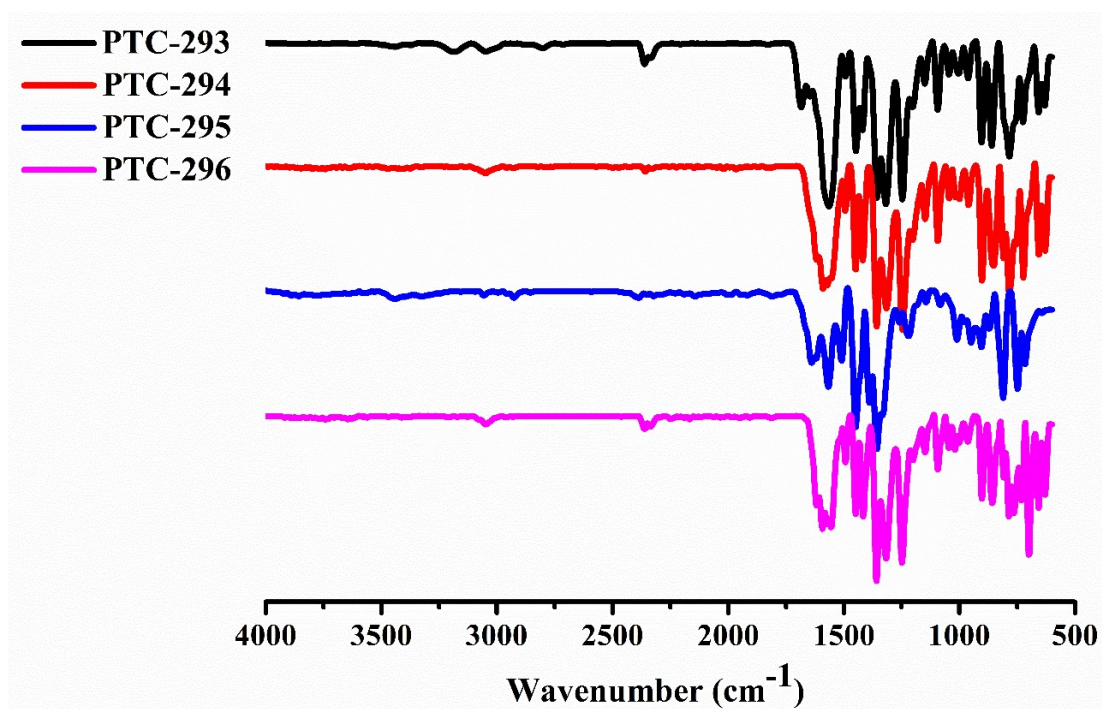
Figure S35. The FT-IR spectra of compounds **PTC-293** to **PTC-296**.

7. The TGA curve of PTCs
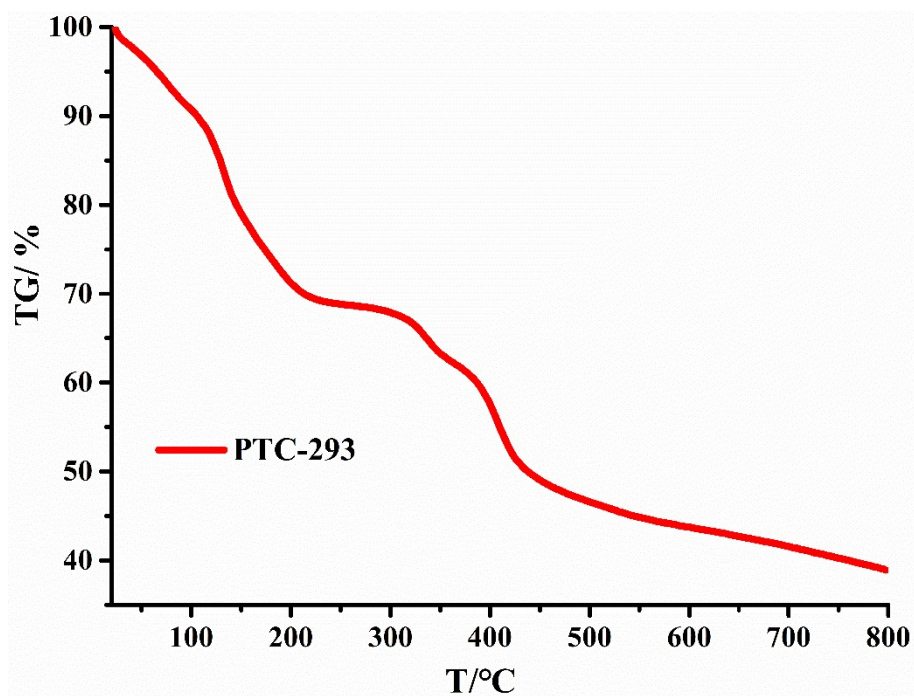
Figure S36. The TGA curve of **PTC-293**.
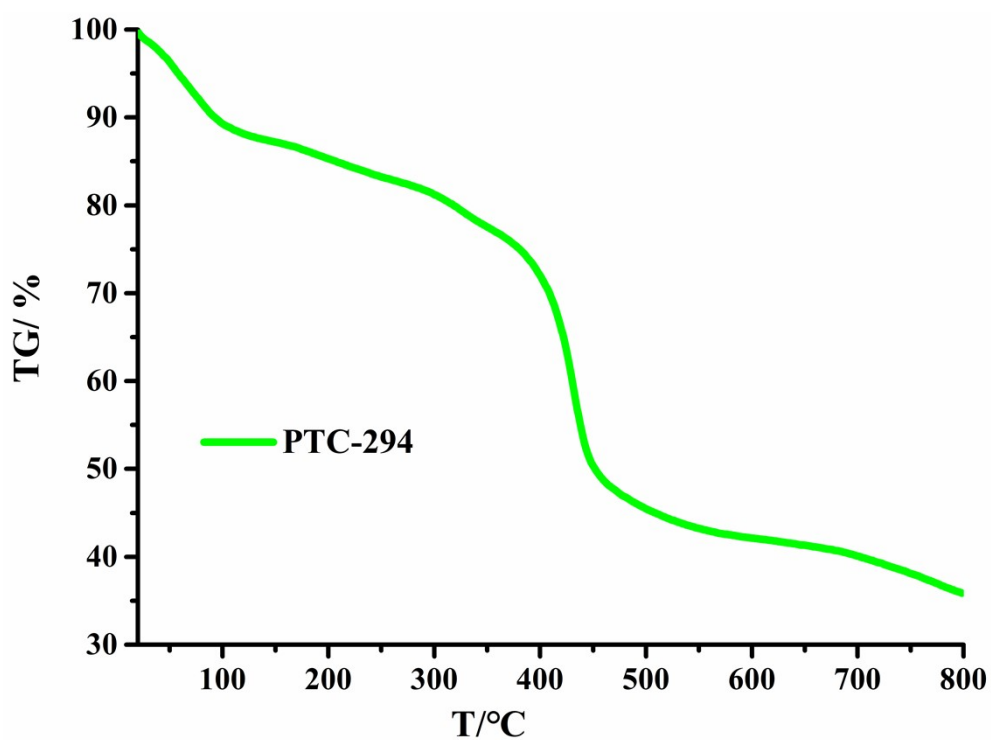
Figure S37. The TGA curve of **PTC-294**.
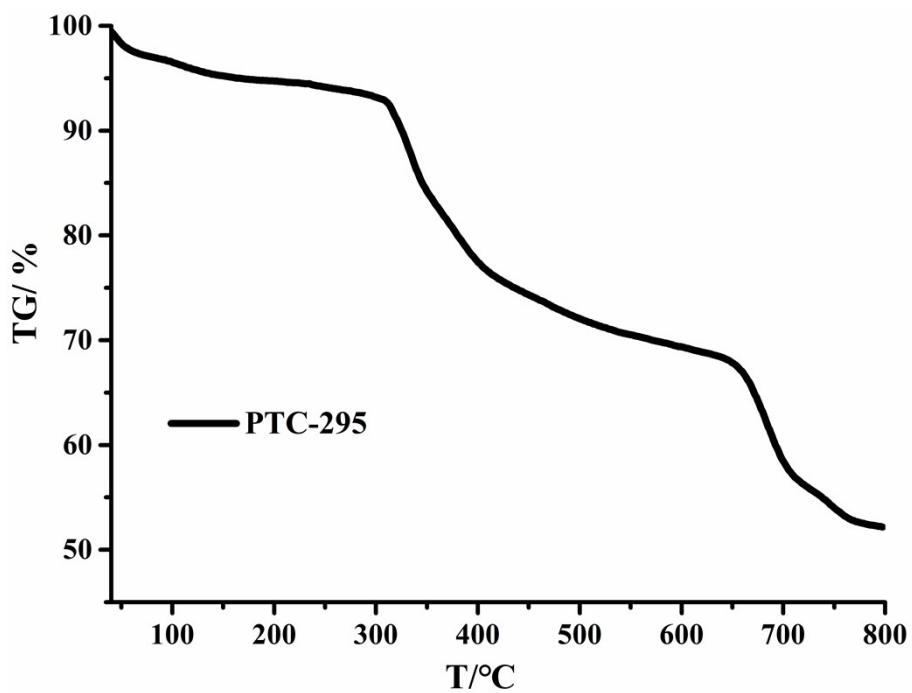
Figure S38. The TGA curve of **PTC-295**.
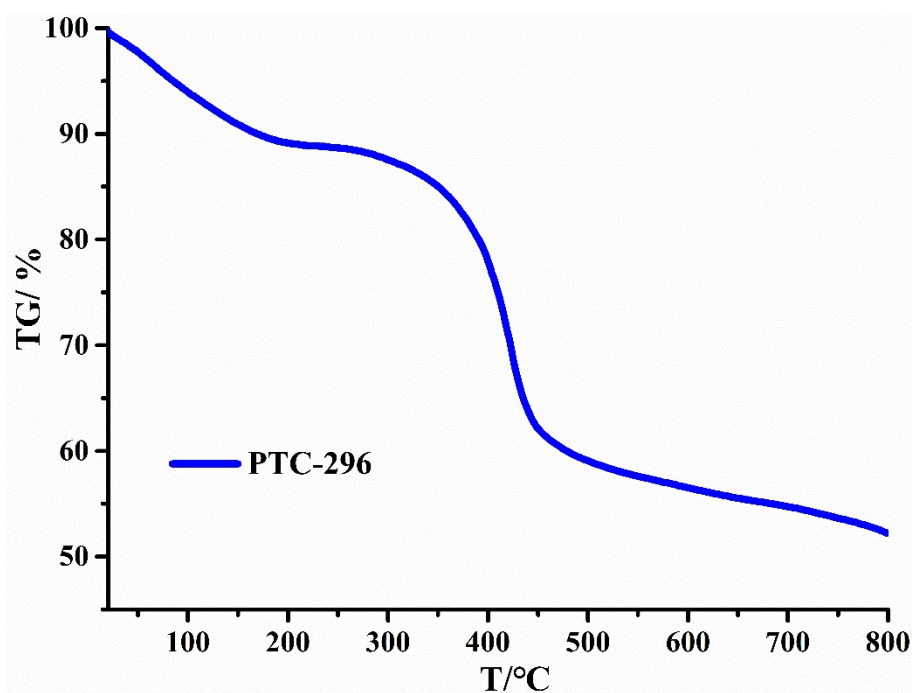
Figure S39. The TGA curve of **PTC-296**.

8. The XPS Spectra of PTCs
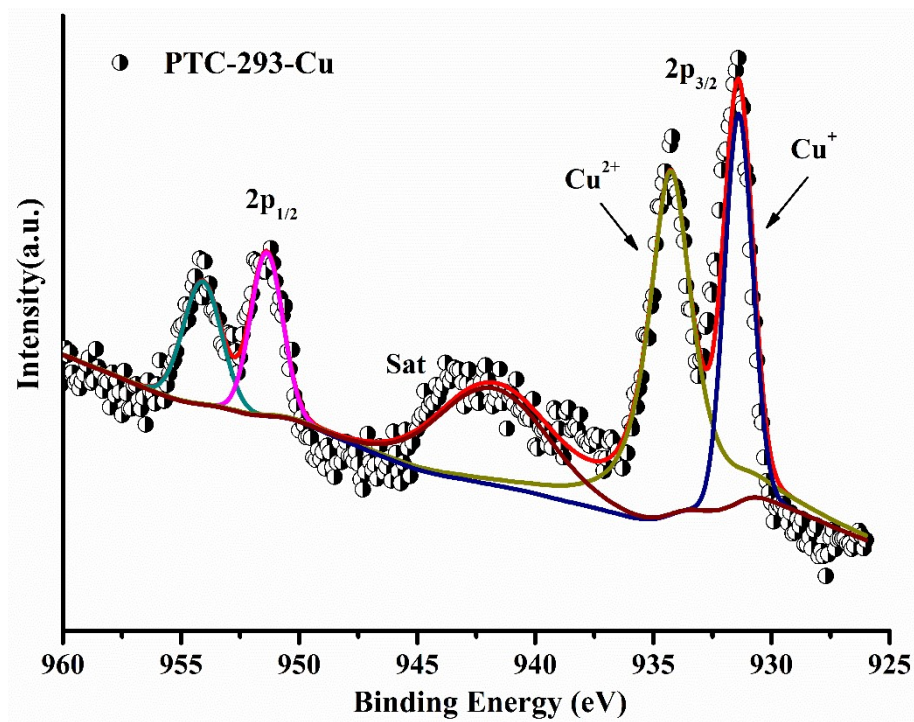
Figure S40. The XPS spectra of **PTC-293-Cu**.
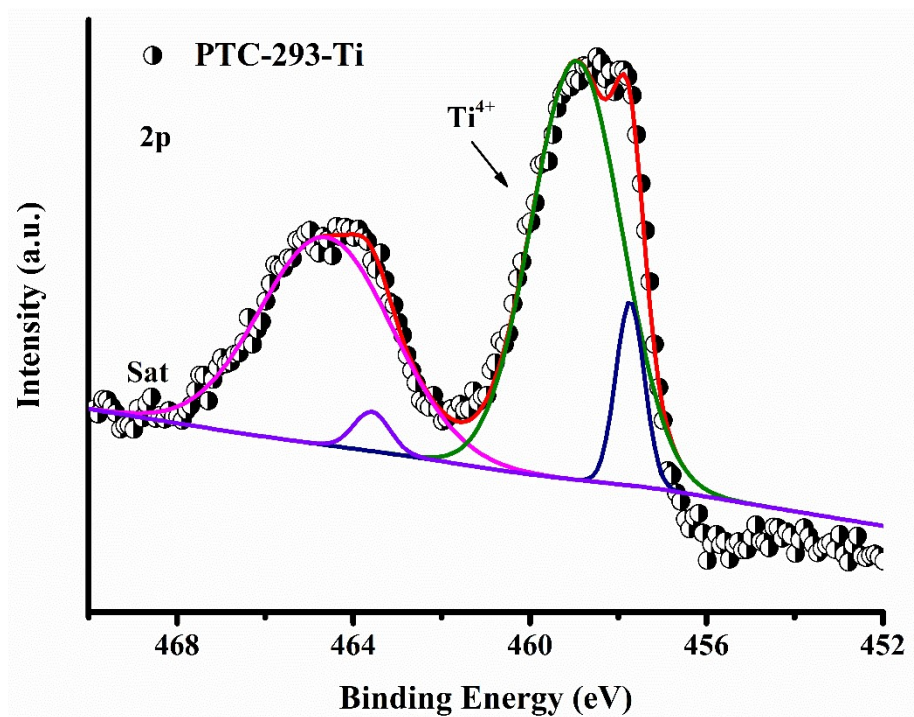
Figure S41. The XPS spectra of **PTC-293-Ti**.
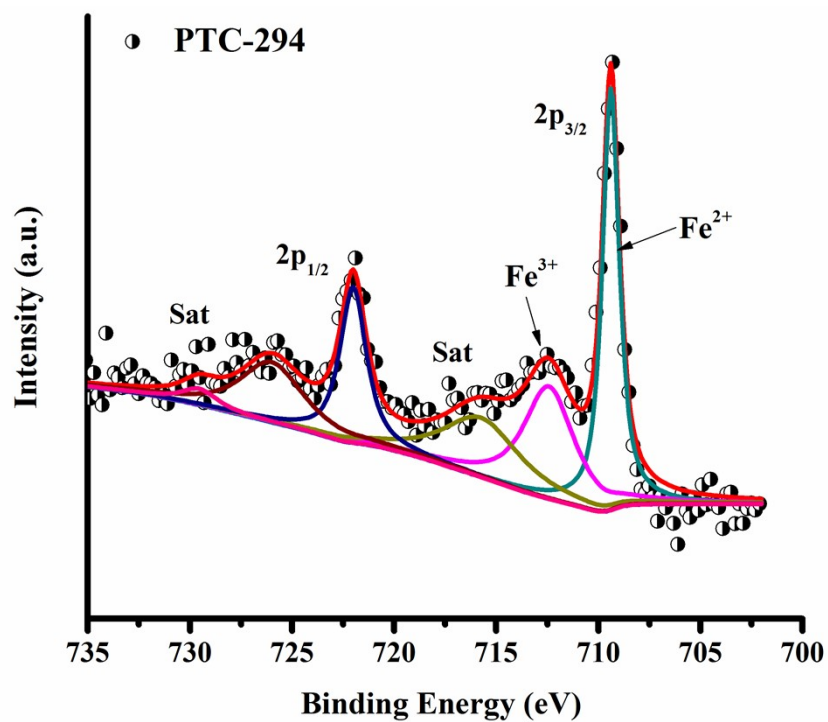
Figure S42. The XPS spectra of **PTC-294**.
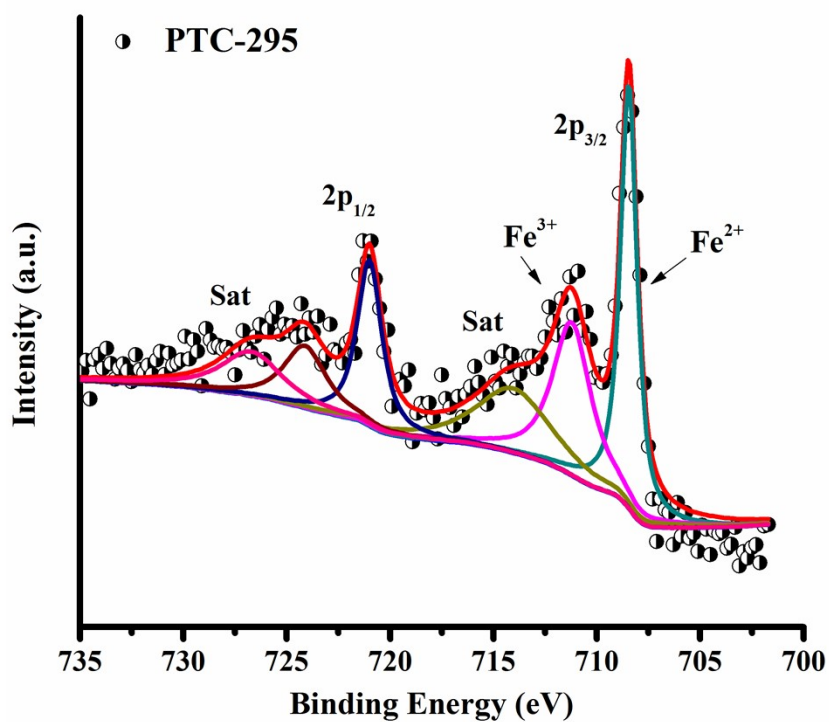
Figure S43. The XPS spectra of **PTC-295**.
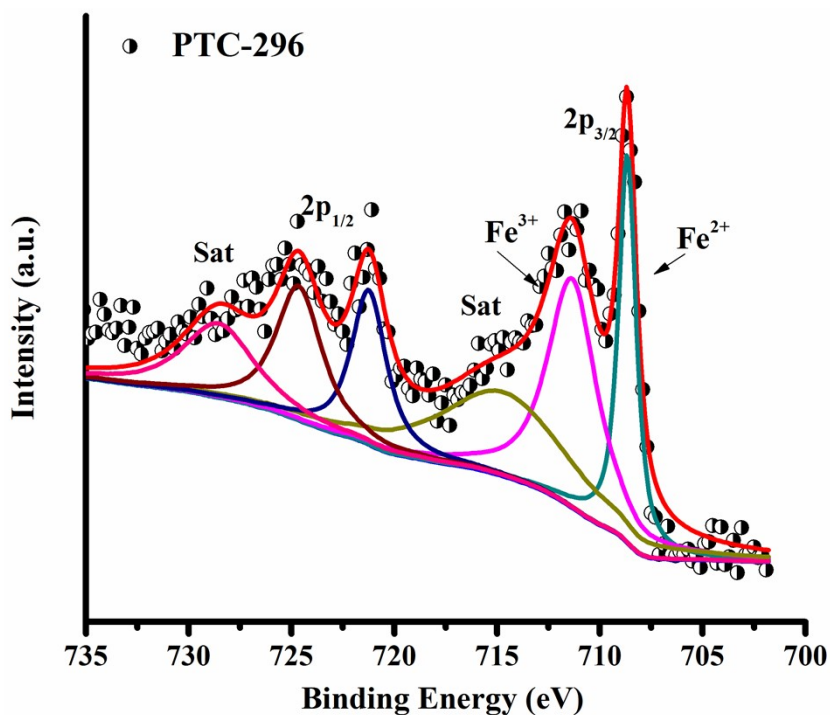
Figure S44. The XPS spectra of **PTC-296**.

X-ray photoelectronspectroscopy (XPS) was used to characterize the Fe oxidation state. It has been shown in previous studies that the peak positions of Fe 2p1/2 and Fe 2p3/2 depend on the ionic states of Fe. In **PTC-294**, all Fe is in the Fe^{2+} state, while in **PTC-295** and **PTC-296**, iron is in mixed price state, but most of them are Fe^{3+} valency. This result is consistent with the raw material of iron.

9. The NLO Property and NICS(0) Method Studies of PTCs
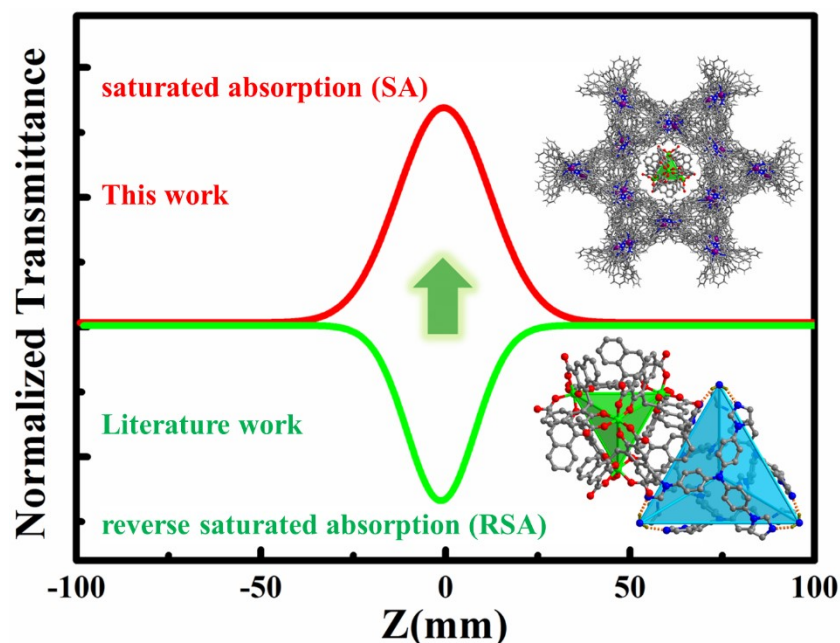
Figure S45. Ti_4(embonate)$_6$-based ionic pairs with tunable nonlinear optics in our reported work and this work.[2]
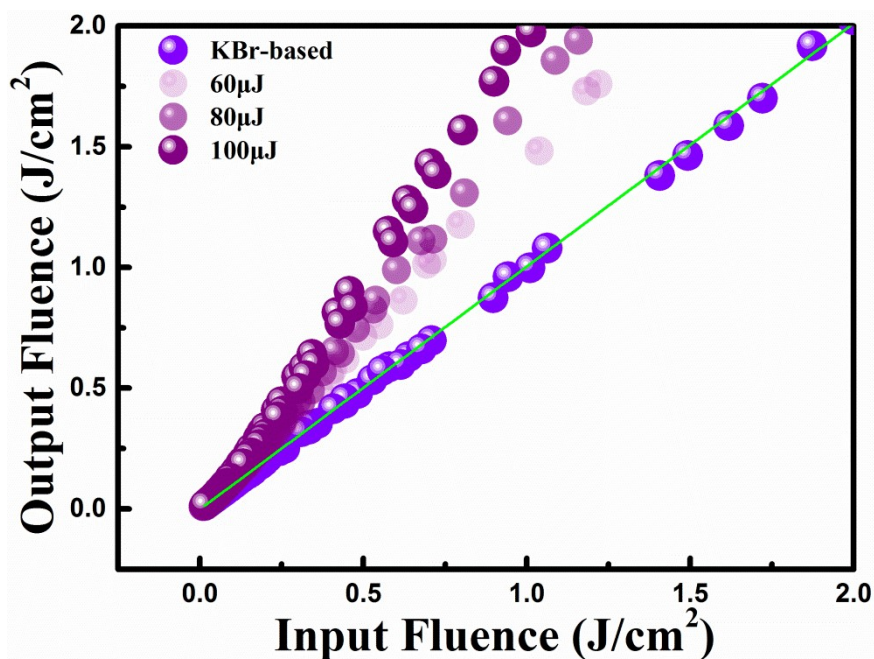
Figure S46. The curves of output fluence versus input fluence for two thin films.

The curves of output fluence versus input fluence of KBr-based thin film and KBr-based **PTC-296** thin film reveal that the output fluence linearly increased at low incident fluence (Figure S46). But at high-incident fluence, the output fluence deviated from linearity represent typical behavior of NLO response for KBr-based **PTC-296** thin film.
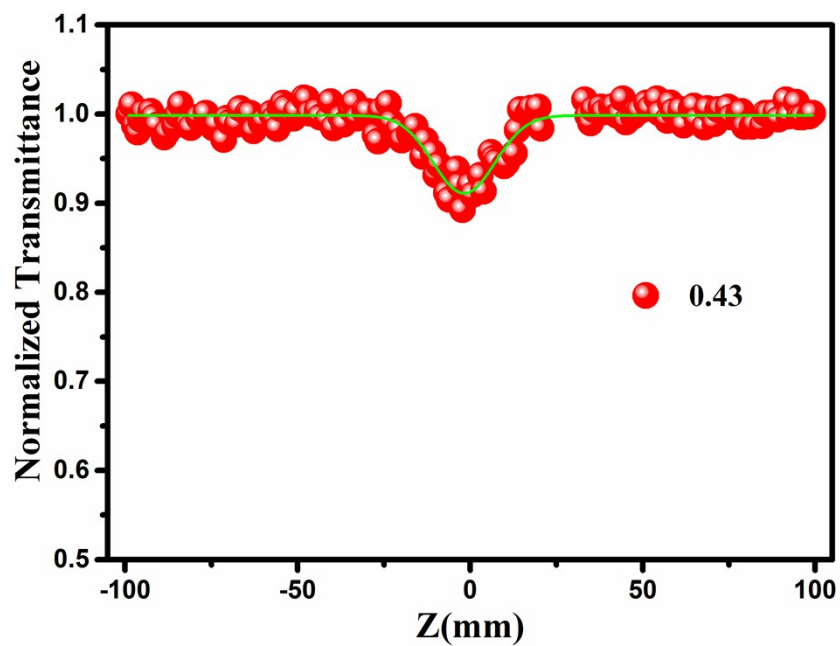
Figure S47. The open-aperture Z-scan results at 532 nm for KBr-based **PTC-293** thin film.
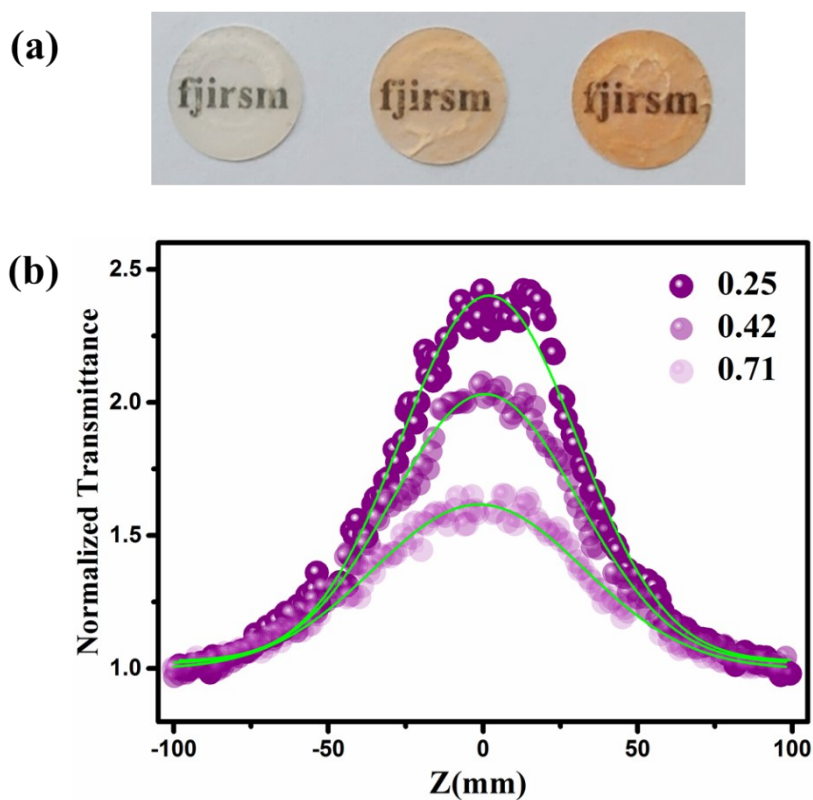
Figure S48. The open-aperture Z-scan results at 532 nm for KBr-based **PTC-294** thin film and the linear transmittance (T_0) was set.
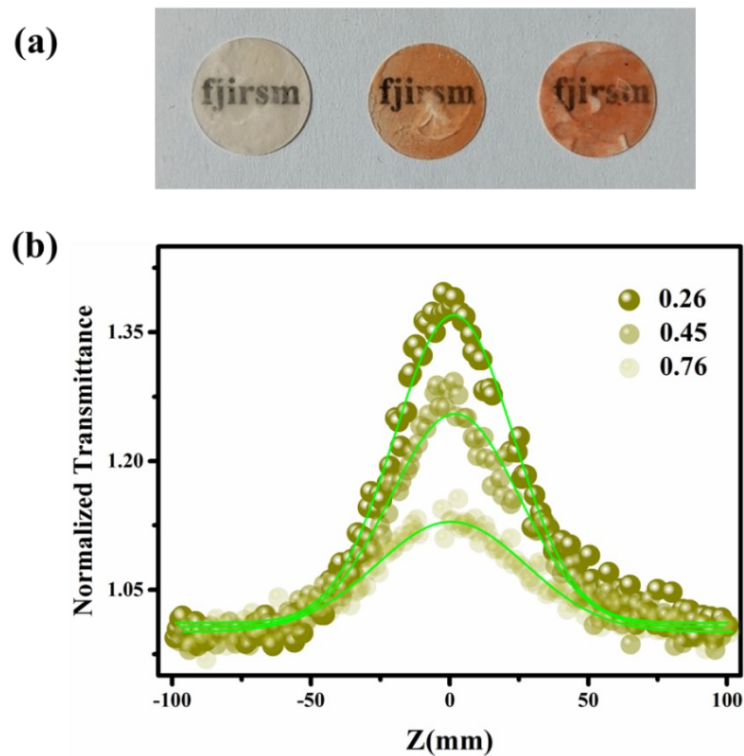
Figure S49. The open-aperture Z-scan results at 532 nm for KBr-based **PTC-295** thin film and the linear transmittance (T_0) was set.
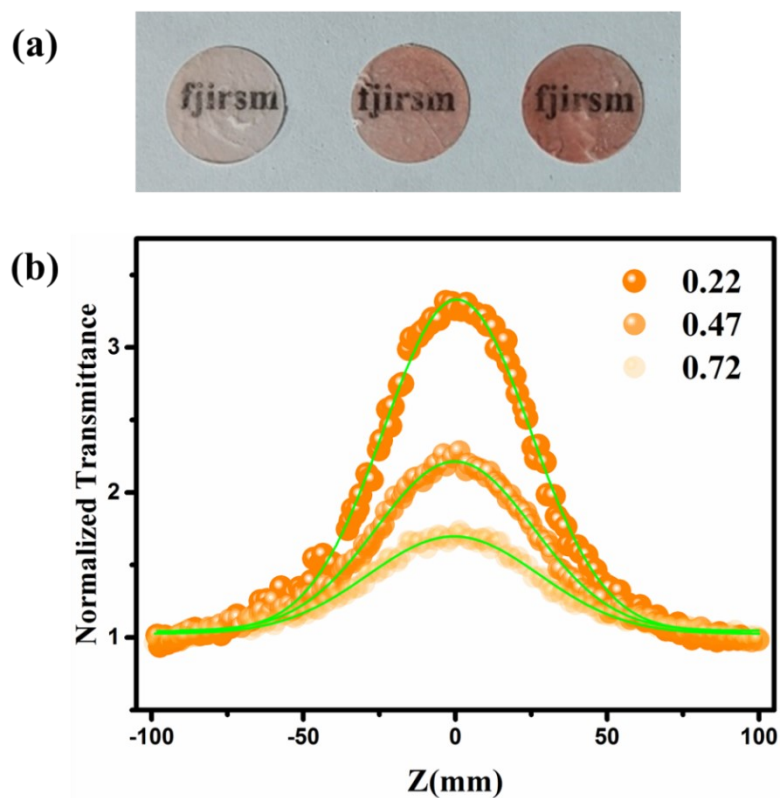
Figure S50. The open-aperture Z-scan results at 532 nm for KBr-based **PTC-296** thin film and the linear transmittance (T_0) was set.

Table S1. Linear, NLO data and NICS(0) values of the samples.

	Linear Transmittance (T_0)	Normalized Transmittance	Nonlinear Absorption Coefficients ($\beta(m/W*10^{-10})$)	Nucleus-Independent Chemical Shift (NICS(0))
PTC-293	0.43	0.91	6.00	-17.19
PTC-294	0.71	1.71	-11.50	-18.42
PTC-295	0.45	1.29	-8.30	-18.46
PTC-296	0.47	2.28	-16.10	-19.37

To test the aromaticity of the selected series of 1,10-phenanthroline type ligands we calculated the Nucleus-Independent Chemical Shift (NICS) values, which has become the most widely applied index to assess aromaticity due to its simplicity and efficiency.[3-5] NICS(0) values are defined as the value of absolute shielding observed at a ring center. Positive NICS(0) values denote antiaromaticity and negative NICS(0) values indicate the presence of aromatic character.

NICS(0) = -17.19 ppm

2,9-Dimethyl-1,10-phenanthroline (Me$_2$phen)

NICS(0) = -18.42 ppm

1,10-phenanthroline (phen)

NICS(0) = -18.46 ppm

3,4,7,8-Tetramethyl-1,10-phenanthroline (Me$_4$phen)

NICS(0) = -19.37 ppm

4,7-diphenyl-1,10-phenanthroline (Ph$_2$phen)
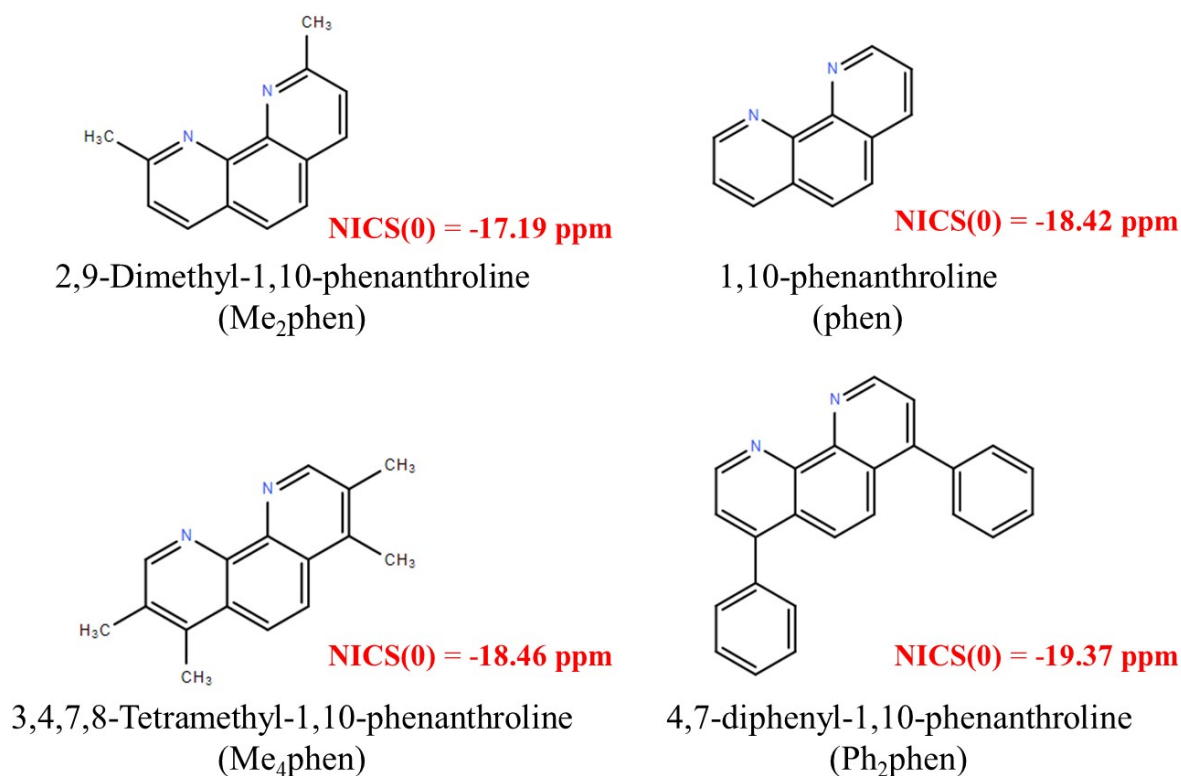
Figure S51. The NICS(0) values for selected 1,10-phenanthroline type ligands.

10. Crystallography Data

Table S2. Crystallographic Data and Structure Refinement Details for **PTC-293** to **PTC-296**.

Compound	PTC-293	PTC-294	PTC-295	PTC-296
CCDC	2107093	2107094	2107095	2107096
Formula	$C_{166}H_{96}CuN_4O_{36}Ti_4$	$C_{225}H_{157}Fe_2N_{17}O_{42}Ti_4$	$C_{250}H_{204}Fe_2N_{16}O_{40}Ti_4$	$C_{446}H_{294}Fe_3N_{34}O_{36}Ti_4$
$D_{calc.}$/ g cm^{-3}	1.124	1.232	1.125	1.209
μ/mm^{-1}	2.176	2.835	2.432	1.426
Formula Weight	2977.60	4073.97	4375.58	7064.36
Colour	orange	crimson	crimson	black
Shape	block	block	block	cube
Size/mm^3	0.30×0.20×0.10	0.30×0.20×0.10	0.30×0.20×0.10	0.30×0.20×0.10
T/K	100.00(19)	99.98(12)	100.00(16)	100.00(11)
Crystal System	monoclinic	triclinic	triclinic	trigonal
Space Group	Cc	P-1	P-1	R-3c
a/Å	31.8045(8)	17.6307(5)	19.8755(10)	40.7336(3)
b/Å	17.8553(3)	19.9692(6)	25.7801(10)	40.7336(3)
c/Å	34.7510(8)	34.0458(9)	25.8788(10)	81.0157(7)
α/°	90	99.561(2)	79.355(3)	90
β/°	116.935(3)	98.330(2)	83.215(4)	90
γ/°	90	108.172(3)	85.683(4)	120
V/Å^3	17593.6(8)	10980.3(6)	12921.2(10)	116413.8(17)
Z	4	2	2	11.99988
Z'	1	1	1	0.333333
Wavelength/Å	1.54184	1.54184	1.54184	1.3405
Radiation type	CuK$_\alpha$	CuK$_\alpha$	CuK$_\alpha$	GaK$_\alpha$
Θ_{min}/°	2.779	2.385	2.240	2.187
Θ_{max}/°	50.436	66.399	64.865	56.909
Measured Refl's.	18376	74929	120694	156225
Indep't Refl's	11000	34861	42767	26453
Refl's I≥2 σ(I)	10225	20925	21067	20850
R_{int}	0.0265	0.0747	0.0986	0.0333
Parameters	1883	2620	2835	1546
Restraints	712	249	444	132
Largest Peak	1.235	0.75	0.79	1.44
Deepest Hole	-0.397	-0.62	-0.78	-0.89
GooF	1.026	1.030	1.075	1.052
wR_2 (all data)	0.1627	0.1835	0.4488	0.3480
wR_2	0.1569	0.1572	0.3807	0.3249
R_1 (all data)	0.0620	0.1136	0.2012	0.1123
R_1	0.0577	0.0647	0.1358	0.0984

11. Reference

1   He, Y.-P.; Yuan, L.-B.; Chen, G.-H.; Lin, Q.-P.; Wang, F.; Zhang, L.; Zhang, J. Water-Soluble and Ultrastable Ti_4L_6 Tetrahedron with Coordination Assembly Function. *J. Am. Chem. Soc.* **2017**, *139*, 16845-16851.

2   He, Y.-P.; Chen, G.-H.; Li, D.-J.; Li, Q.-H.; Zhang, L.; Zhang, J. Combining a Titanium–Organic Cage and a Hydrogen-Bonded Organic Cage for Highly Effective Third-Order Nonlinear Optics. *Angew. Chem. Int. Ed.* **2021**, *60*, 2920-2923.

3   Williams, R. V.; Armantrout, J. R.; Twamley, B.; Mitchell, R. H.; Ward, T. R.; Bandyopadhyay, S. A Theoretical and Experimental Scale of Aromaticity. The First Nucleus-Independent Chemical Shifts (NICS) Study of the Dimethyldihydropyrene Nucleus. *J. Am. Chem. Soc.* **2002**, *124*, 13495-13505.

4   Ozer, M. S.; Menges, N.; Keskin, S.; Sahin, E.; Balci, M. Synthesis of Pyrrole-Fused C,N-Cyclic Azomethine Imines and Pyrazolopyrrolopyrazines: Analysis of Their Aromaticity Using Nucleus-Independent Chemical Shifts Values. *Org. Lett.* **2016**, *18*, 408-411.

5   Pagano, J. K.; Xie, J.; Erickson, K. A.; Cope, S. K.; Scott, B. L.; Wu, R.; Waterman, R.; Morris, D. E.; Yang, P.; Gagliardi, L.; Kiplinger, J. L. Actinide 2-metallabiphenylenes that satisfy Huckel's rule. *Nature* **2020**, *578*, 563-567.